NTNU

Norwegian University of
Science and Technology

Simulation of Ductile Crack Propagation in Steel Pipes

Mari Skarstein
Elise Sterner

Department of Structural Engineering
FACULTY OF ENGINEERING SCIENCE
NTNU – Norwegian University of Science and Technology

MASTER'S THESIS 2018

for

Mari Skarstein and Elise Sterner

Simulation of Ductile Crack Propagation in Steel Pipelines

Safe transport of gases and liquids in steel pipelines implies that rupture of the pipe should be avoided in the advent of an accident. A crack in a pressurized pipe may start to propagate rapidly along the pipeline and run for long distances. Modern steel pipes are ductile and this phenomenon is denoted running ductile failure. The crack will propagate as long as the pressure level at the crack tip is sufficiently high for the ductile failure processes to occur.

In this study, solid element analyses shall be used to simulate ductile failure and running ductile failure in a pipeline with an initial crack. The material behaviour shall be described by the Gurson model that accounts for plasticity and damage evolution. The Gurson model shall be calibrated based on materials tests on an X65 pipeline steel. The solid element analyses shall be used to develop a failure criterion or cohesive law that can be used in shell element simulation of running ductile fracture in pipelines. These simulations shall be validated against existing experimental data from the literature.

The main tasks of the research project are as follows:

1. To perform a literature review on experiments and modelling of running ductile failure in steel pipelines.
2. To complete an experimental study to characterize the plastic behaviour and the ductility of an X65 pipeline steel at various stress states, using standard tensile tests, notched tensile tests and Kahn tearing tests.
3. To calibrate the Gurson model for ductile failure of the X65 steel.
4. To run simulations of the materials tests performed in the laboratory to validate the calibrated constitutive model.
5. To establish a solid element model for running ductile failure in a small part of a steel pipeline.
6. To apply the solid element model to develop a failure criterion or cohesive law for pipeline steel.
7. To establish a model of the pipeline with the developed failure criterion/cohesive law and to perform simulations of running ductile failure in pipelines.
8. To report the research work.

Supervisors: Odd Sture Hopperstad, Tore Børvik, Sondre Bergo

The report should be written in the style of a scientific article and submitted to the Department of Structural Engineering, NTNU, no later than June 11, 2018.

NTNU, January 15th, 2018

Odd Sture Hopperstad
Professor

Abstract

For the transport of gases and liquids, such as CO_2, in steel pipelines to be safe, rupture in the pipe should be avoided. A crack in a pressurized pipe may start to propagate rapidly along the pipeline and run for long distances. Modern steel pipes are ductile and this phenomenon is denoted running ductile failure. The crack will propagate as long as the pressure level at the crack tip is sufficiently high for the ductile failure processes to occur.

In this study, solid element analyses were used to simulate ductile failure and running ductile failure in a part of a pipeline with an initial crack. The material behaviour of X65 steel was first established by quasi-static tension tests on different notched specimens, and parameters for a Gurson-Tvergaard-Needleman (GNT) model were calibrated through inverse modelling in Abaqus. The developed GTN model was then validated for a Kahn tearing test using the same X65 steel, and the phenomenon of tunneling in the Kahn tests was studied using X-ray computed tomography (CT). As the GTN model was found able to represent fracture in the tearing test, it was then used to establish fracture energy and nominal stress parameters for a Cohesive Zone (CZ) model. This was then used to perform a solid element analysis on a part of a pipeline using a simplified load case. The CZ model was found to be able to represent the fracture in a sufficient manner, but the crack length in the pipe proved to be dependent on the global element size used in the simulations. A GTN model was also established for a part of the pipeline, and was found to represent the fracture in a similar manner as the CZ model.

For further studies a numerical model of the pipe could be developed where the pressure is applied as a function of the position of the crack tip, and to validate the model by comparing it to a fluid structure model. A less mesh-sensitive non-local GTN model could also be established.

Abstract

For at transport av gasser og væsker, som for eksempel $CO2$, i stålrør skal være trygt bør brudd i røret unngås. En sprekk i røret kan begynne å propagere veldig raskt langsmed røret og bevege seg over lange avstander. Dette fenomenet betegnes som et duktilt løpende brudd. Sprekken vil fortsette å vokse så lenge trykknivået ved sprekkspissen er høyt nok til at den duktile bruddprosessen oppstår.

I denne studien ble elementmetodeanalyser brukt til å simulere duktilt brudd og løpende duktilt brudd i en liten del av en rørledning med en påsatt liten sprekk. Materialet var X65 stål, og materialets oppførsel ble først etablert ved kvasi-statiske spenningstester på forskjellige kjervede prøver, og parametere for en Gurson-Tvergaard-Needleman (GNT) -modell ble kalibrert gjennom invers modellering i Abaqus. Den utviklede GTN-modellen ble deretter validert for en Kahn-rivningstest med samme X65-stål, og fenomenet tunneling i Kahn-testene ble undersøkt ved hjelp av et røntgenbasert datamatografi (CT) -studie.

Siden GTN-modellen ble bevist å kunne representere brudd i rivningstesten, ble den deretter brukt til å etablere bruddkraft og nominelle stressparametere for en kohesiv sone (CZ) modell. Dette ble så brukt til å utføre en elementmetodeanalyse på en liten del av en rørledning ved hjelp av en forenklet belastningssituasjon. Det ble funnet ut at CZ modellen kunne representere brudd på en tilstrekkelig måte, men sprekklengden viste seg å være avhengig av den globale elementstørrelsen som ble brukt i simuleringene. En GTN-modell ble også etablert av en del av rørledningen, og det ble bevist at den kunne representere bruddet på en lignende måte som CZ-modellen.

For videre studier burde en numerisk modell av røret utvikles der trykket påføres som en funksjon av sprekkens spiss, og for å validere modellen burde den sammenlignes med en fluid-struktur modell. En mindre mesh-følsom ikke-lokal GTN modell kan også etableres.

Preface

This thesis was written spring 2018 at the Structural Impact Laboratory (SIMLab), located at the Department of Structural Engineering at the Norwegian University of Science and Technology (NTNU). The thesis was the final work of the Master of Science degree in Mechanical Engineering at NTNU, with specialization in Applied Mechanics. The work was done under the supervision of Professor Odd Sture Hopperstad, Professor Tore Børvik and PhD Candidate Sondre Bergo at the SIMLab.

Acknowledgements

Table of Contents

Abbreviations

BLR	=	Bridgman-LeRoy
BTCM	=	Battelle Two Curve Method
CCS	=	Carbon Capture and Storage
CFD	=	Computational Fluid Dynamics
CL	=	Cockroft-Latham
CPU	=	Central Processing Unit
CT	=	(X-Ray) Computed Tomography
CTOA	=	Crack Tip Opening Angle
CTOD	=	Crack Tip Opening Displacement
CZ	=	Cohesive Zone
DIC	=	Digital Image Correlation
DWT	=	Drop-Weight Test
FE	=	Finite Element
GTN	=	Gurson–Tvergaard–Needleman model
RDF	=	Running Ductile Fracture

Chapter 1

Introduction

1.1 Motivation

One of the most significant contributors to climate changes in the world today is the emission of CO_2. A cornerstone of the drive to reduce CO_2 emissions is the use of Carbon Capture and Storage (CCS) (Mahgerefteh et al., 2012). This involves capturing CO_2 from large industrial emitters, such as coal and gas-fired power stations, and transporting it to permanent storage sites, such as depleted oil or gas reservoirs or saline aquifers. For this, the most widely recognised mean of transporting vast amounts of captured CO_2 are pressurised pipelines, and these pipelines may typically cover distances of several hundred kilometres at high pressures.

However, today's knowledge of the behaviour of these CO_2 pipelines is not sufficient to safely guarantee that running fractures in the pipelines will not happen. A running fracture in these pipelines is considered catastrophic failure and involves rapid tearing of the pipeline that can sometimes run for several hundred meters, which results in the release of massive amounts of content in a very short space of time. If these pipelines are passing through or near populated areas, the consequences will be especially fatal, and so a large number of studies have been devoted to understanding the mechanism of these running fractures over a span of more than 30 years.

Reasons for the fracture can be defects introduced into the pipe by outside forces such as mechanical damage, soil movement, corrosion or material defects. These defects will be subjected to stresses, and when these stresses overcome the fracture toughness of the pipe, the fracture will propagate. For CO_2 especially, which has an unusually high saturation pressure, pipelines transporting the gas will be more susceptible to fracture propagation, compared to hydrocarbon pipelines. Current methods, developed about 40 years ago, use semi-empirical models based on the Battelle Two Curve Method (BTCM). When this approach is applied to today's high toughness steels or using non-ideal gases such as CO_2, the results have shown to be unreliable and inaccurate (Nordhagen et al., 2014), and are therefore non-applicable. The solution: new methods need to be developed.

1.2 Literature study

Fracture mechanics

The behaviour of metals/alloys is important to understand, as they are widely used as structural materials. A structural component fails when the material loses its load-bearing capacity. Failure is commonly classified into either brittle or ductile failure. Brittle materials experience only elastic deformation before fracture, while ductile materials deform plastically before fracture. When fracturing, brittle materials shatter, while ductile materials can be bent and remain in its new shape. Ductile materials require more work than brittle materials to propagate a crack because the energy is being absorbed by the plastic deformation. This big difference between brittle and ductile materials is because elastic deformation stores energy, while plastic deformation dissipates it.

During the fracture process, ductile materials demonstrate a wide range of fracture behaviour due to the interaction of plastic energy absorption. Material fracture mechanics involves predicting the fracture behaviour from the material microstructure and material properties. Most of the early work developed to predict crack-tip conditions were based on a global approach using energy methods where the material was regarded as a continuum. These methods used singe parameters to predict the crack-tip conditions and are mostly used for brittle fracture (Anderson, 2005). In the case of ductile failure and fracture, the microscopic mechanisms have to be considered.

Modelling of ductile failure and fracture

When structural steel is subjected to high plastic strains, ductile fracture is the most common fracture initiating mechanism. Ductile fracture is governed by void nucleation, growth and coalescence. Poro-mechanics is a branch of continuum mechanics, where the behaviour of a porous media, i.e. a material matrix permeated with micro-voids is studied. An essential parameter when modelling the behaviour of a porous media is the void volume fraction. The void volume fraction is essentially a damage parameter employed in the constitutive equation that interacts with other state variables. Such models are classified as a coupled approach, as it allows the yield surface to be altered by the damage evolution.

In 1968, McClintock developed a quantitative fracture criterion for fracture by the growth and coalescence of preexisting holes in plastic materials. This was done by analysing the expansion of a long circular cylindrical cavity in a non-hardening material, pulled in the direction of its axis while subjected to transverse tensile stresses. It was found that in plastic materials, the inverse dependence of fracture strain on hydro-static tension was very strong (A. McClintock, 1968). In 1969, Rice & Tracey determined another approximate solution by considering an isolated spherical void in a uniform stress and strain-rate field (Rice and Tracey, 1969), where the relation between void growth and stress triaxiality was their focus. In 1975 Gurson provided a constitutive relation from a progressively cavitating solid with void growth based on Rice & Tracey (Rice and Tracey, 1969).

Tvergaard, and later Tvergaard & Needleman made modifications of the Gurson relation to improve void growth modelling and account for coalescence. This resulted in the Gurson-Tvergaard-Needleman (GTN) model, which is the most widely used coupled approach for modelling void growth. (Tvergaard, 1981), (Tvergaard, 1982), (Tvergaard and Needleman, 1984).

Modelling of running ductile fracture in pipes

When modelling the propagation of a crack in a pipe, the most challenging part is the modelling of the pressure distribution throughout the pipe and the lack of experimental data for comparison.

Coupled CFD-FE models have been investigated at SINTEF, where the results have been compared to experimental data. Nordhagen et al. compared experimental data to a coupled fluid-structure model in LS-DYNA, pressurised with methane and hydrogen. Nordhagen et al. used shell elements to model the pipe with X65 steel material. The crack propagation was described by element erosion with the Cockroft-Latham ductile fracture criterion that depends on the principal stress and equivalent plastic strain (Nordhagen et al., 2012). Crucial for the performance of the coupled model was the description of the pressure profile in the vicinity of the crack tip. The pressure profile depended on the position of the crack tip and the size of the crack opening so that there was a two-way coupling between the structure model and the fluid. When comparing with full-scale experiments, it was clear that Nordhagen et al. were successful in describing both the pressure evolution in front of the running ductile fracture and the crack position.

Nordhagen et al. (Nordhagen et al., 2014) also did a study on the main properties governing the ductile fracture velocity in pipelines, with a similar CFD-FE model to the one used in the previous study by Nordhagen et al. (Nordhagen et al., 2012). Compared to the previous study, the fluid model was more simplified to increase the efficiency of the study. Strong mesh sensitivity was observed in the numerical model using shell elements. They proposed to use solid elements to capture necking, as necking might be a driving force for the fracture velocity. They found that the average crack speed was most sensitive to pipe thickness, followed by initial pressure, Cockcroft-Latham fracture parameter, decay length, yield strength, pipe diameter and work-hardening (Nordhagen et al., 2014).

Aursand et al. (Aursand et al., 2016) and Nordhagen et al. (Nordhagen et al., 2017) developed coupled fluid-structure numerical models especially considering the transportation of CO_2-rich mixtures in steel pipelines. Aursand et al. observed good agreements for pressures, crack lengths and fracture velocities compared to experimental data. It was found from simulations that the pressure levels behind the crack tip were different compared to natural-gas pipelines (Aursand et al., 2016). Nordhagen et al. investigated the effect of the pipes being surrounded by water or buried in soil, as this would decrease the speed of the running ductile fracture. They achieved good agreements between the experimental results and the simulations for the pressure along the pipes, while the numerical model gave conservative results of the crack lengths, and varying results for the crack velocities for the different CO_2 mixtures (Nordhagen et al., 2017).

FE models without a fluid coupling, describing the pressure instead as a function of the position of the crack tip have also been investigated. When combining fluid and structural models, the challenges concerning mathematical modelling, numerical discretisation, solution techniques, and realisation as software tools on modern computer architecture are still huge (Belostosky et al., 2014). Several studies concern the modelling of running ductile fracture using only solid structural models. Modelling the crack path with a cohesive zone (CZ) is essential in these studies.

Hutchinson & Nielsen analysed a method to characterise the traction - separation behaviour of a mode I crack in a 2D plane strain finite element model, and to further find the

cohesive fracture energy of the entire failure process. They showed how the energy in the traction - separation curve could be divided into two parts, the dissipated energy between the onset of necking and the onset of shear localisation, and the dissipated energy after the onset of shear localisation. The energy dissipated between the onset of necking and the onset of shear localisation defined the damage evolution in the model. They found that the damage evolution found from the numerical model was mesh independent up to shear localisation. When studying the local necking, shear localisation and final slant failure, they found that the three most important parameters influencing the cohesive energy were the initial void volume fraction, the shear coefficient and the strain hardening (Hutchinson and Nielsen, 2012).

Völling et al. developed an FE model of a pipe to investigate crack propagation and fracture velocity for a BTCM based prediction of crack arrest. A CZ model was used to simulate ductile failure, where the CZ parameters were determined from laboratory tests using a tearing test of type drop-weight test (DWT) specimen. The pressure decay behind the crack tip on the flaps was modelled using a function dependent on the position of the crack tip, while the pressure in front of the crack tip was kept constant. Völling et al. conducted a parameter study on the relation between global pressure and local pressure decay on the flaps, and the corresponding crack velocity. It was found that the DWT test specimens were recommended for the calibration of damage parameters, where no adjustments needed to be done. Völling et al. justified that the behaviour in DTW test specimens and the pipe had similar stress-strain conditions and that the direct transferability of parameters between the DTW model and the pipe model was valid (Dr Alexander Völling, 2013).

Nonn & Kalwa compared the use of GTN model and the CZ model to experimental data in numerical DTW models on X65 and X80 steel, where they characterised the ductile damage behaviour. They calibrated the GTN model from notched tensile tests, where the parameters found for the GTN model were the void volume fraction, the critical porosity, the volume fraction of secondary voids and the characteristic element size. The CZ parameters were calibrated and verified from a numerical DTW model. They found that the most relevant parameters with regards to the GTN model were the volume fraction of secondary voids and the element size (Nonn and Kalwa, 2013).

Scheider et al. (Scheider et al., 2014) modelled the crack propagation in the pipeline also applying the pressure as a function of the position of the crack tip. Two numerical pipe models were used to simulate the crack propagation, one with a GTN model, and one with a CZ model. The calibration procedure involved notched tensile specimens and the DWT test, justified by Völling et al. (Dr Alexander Völling, 2013). For the CZ model, the calibrated parameters were the cohesive strength and the cohesive energy. For the GTN model, only the two parameters volume fraction of secondary voids and the element size was calibrated, as Nonn & Kalwa (Nonn and Kalwa, 2013) found these parameters to be most relevant ones. It was found that both of the CZ model and the GTN model were suitable to describe the dynamic fracture resistance. The computational efficiency was low for the GTN model, while the CZ model was found to represent more robust solutions concerning this matter.

1.3 Background

This thesis is an extension of the thesis of Gry Hellum from 2017 (Hellum). In her thesis, Hellum studied the main effects and interaction effects of temperature, strain rate and stress triaxiality on an offshore X65 steel. Hellum performed tensile tests on smooth and notched specimens using X65 steel. The results were used to calibrate the material parameters for a Johnson-Cook model, where Power law was used as the hardening model. These were used in numerical models of the specimens in Abaqus/Standard and Abaqus/Explicit, and it turned out that the models were able to produce the same results as the experiments for the smooth specimen, but overestimated the stress level for the notched specimens. This was not investigated further in Hellum's thesis.

The experimental results from the smooth and notched tensile tests conducted by Hellum, and the work-hardening parameters, will be used in this thesis. Also, the overestimation of the stress level for the notched specimens will be investigated further by taking into account void growth by using the GTN yield criterion. Hellum also proposed to use edge-tracing to find the diameter reduction in order to calculate true stress and logarithmic strain for the tensile tests. In this thesis, additional tensile tests will be conducted using high-resolution cameras to be able to perform edge-tracing on the results.

The validation of the found parameters for the GTN model will be done using Kahn tearing tests. This is a tearing test that resembles the DWT test used in several previous studies when modelling a pipe, because of the transferability between the stress-strain conditions of the DWT test and the pipe. The studies done by Völling et al., Nonn & Kalwa and Schneider et al. used the DWT test as validation of the material model to calibrate cohesive properties of a CZ model, giving good results (Dr Alexander Völling, 2013), (Nonn and Kalwa, 2013), (Scheider et al., 2014).

Few studies have been done on the use of steel Kahn tearing tests, but the applicability should be similar to that of the DWT test. If the GTN model is validated by describing the behaviour in the Kahn test well, a ductile fracture in a pipe may be described by this model also.

1.4   Objectives & scope

Objective

The objective of this thesis is to present a methodology that can be used for the assessment of pipeline fracture resistance against long-running ductile fracture.

The sub-objectives are as follows:

1. Literature study on experiments and modelling of running ductile failure in steel pipelines.

2. Completion of an experimental study to characterise the plastic behaviour and the ductility of X65 pipeline steel, using standard tensile tests, notched tensile tests and Kahn tearing tests.

3. To calibrate the GTN model for ductile failure of the X65 steel.

4. To run simulations of the material tests in the laboratory to validate the calibrated GTN model.

5. To establish a solid element model for running ductile failure in a small part of a steel pipeline.

6. To apply the solid element model to develop a cohesive law for pipeline steel.

Scope

The scope of this thesis is as follows

1. The experimental study was only performed on X65 steel.

2. The experimental study was only performed on five different specimen geometries; 4 tensile tests and the Kahn tearing test.

3. The experimental tests used were only performed at room-temperature. Other temperatures were not considered for this study.

4. Only quasi-static behaviour was considered, not dynamic.

5. Only an FE model was used in this thesis to simulate a running failure. A CFD-FE model was not used to represent fluid-structure interaction.

1.5   Overview of thesis

Chapter 2: Material Mechanics

Chapter 2 introduces the plasticity theory used in this thesis and relevant instability damage and fracture mechanics.

Chapter 3: Material tests and simulations

In chapter 3, parameters for the GTN model were calibrated by developing numerical models for comparisons with experimental quasi-static tension test performed on X65 steel. Parameters found were the initial void volume fraction, critical and total void volume fraction as well as mesh size for the GTN model. The geometry of the specimens was proved to be of great importance for the correlation between numerical and experimental results, and a Python script was developed with the purpose of tracking the specimen geometry.

Chapter 4: Tearing tests and simulations

In chapter 4, experimental Kahn tearing tests were performed. The force-elongation curve was measured using Digital Image Correlation (DIC), and X-ray computed tomography (CT) was performed on the deformed specimens to observe tunnelling in the specimens. A numerical GTN model was then established for the Kahn-test and compared to experimental data. The GTN model was found to be able to represent the Kahn tearing test.

Chapter 5: Pipe simulation

In chapter 5, a numerical GTN model was established to calibrate parameters for a CZ model. A numerical GTN model was first used to establish CZ parameters for a Kahn tearing test for validation. CZ parameters for a pipe were then found, and two numerical models of a part of a pipe were established. A parameter study was done on these models. A GTN model of the pipe was also established and compared to the CZ models.

Concluding remarks

In Concluding remarks, the most important results and conclusions are summarised, and some suggestions for further work are presented.

Chapter 2

Material Mechanics

In the following sections, some basic theory regarding the material model will be presented. More specific theoretical aspects will be covered later locally in each chapter when needed.

2.1 Plasticity

In this section the three parts of plasticity-theory will be covered, the yield criterion, the flow rule and the work hardening rule. The GTN model, which will be explained in section 2.2.3 is an extension of the von Mises yield criterion and is represented by the von Mises yield criterion if zero voids and zero nucleation is assumed in the material. The von Mises yield function will therefore be introduced in the first section of the plasticity theory. The associated flow rule and the Power Law will then be covered.

2.1.1 Yield criterion

A yield criterion expresses the condition for the onset of plastic deformation, and it is defined in terms of the stress components. In general, it is formulated as:

$$f(\boldsymbol{\sigma}) = \varphi(\boldsymbol{\sigma}) - \sigma_Y = 0 \tag{2.1}$$

where f is the yield function, φ is the equivalent stress (represented by a positive homogenious function of order one) and σ_Y the yield stress which represents the stress at yielding in uniaxial tension.

The von Mises yield criterion

One of the perhaps simplest and widely used yield criterion is the von Mises criterion. It is based on the assumption of plastic isotropy and pressure insensitivity, i.e. yielding is independent of the hydrostatic stress σ_H. Thus, yielding of the material is only dependent

on the deviatoric part of the stress state $(\sigma_1, \sigma_2, \sigma_3)$ (Hopperstad and Børvik, 2017a). The von Mises criterion may be written as:

$$f(\boldsymbol{\sigma}) = \sqrt{3J_2} - \sigma_Y = 0 \qquad (2.2)$$

The von Mises yield criterion can be plotted as a surface in the principal stress space. This is defined as a coordinate system defined by the principal stresses $\sigma_1, \sigma_2, \sigma_3$, and the yield surface ($f=0$) is a circular cylinder centred on the hydrostatic axis. This is defined by $\sigma_1=\sigma_2=\sigma_3=\sigma_H$. Figure 2.1 illustrates the von Mises yield surface in the principal stress space $(\sigma_1, \sigma_2, \sigma_3)$.
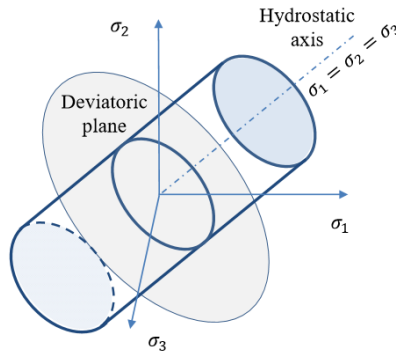

Figure 2.1: von Mises yield surface in the principal stress strate, Figure from (Hopperstad and Børvik, 2017a).

2.1.2 Flow rule

$$\dot{\varepsilon}^p_{ij} = \dot{\lambda} \frac{\partial g}{\partial \sigma_{ij}} \qquad (2.3)$$

The plastic flow rule in equation 2.3 defines $\dot{\varepsilon}^p_{ij}$ in a way that ensures non-negative plastic dissipation $D_p = \sigma_{ij}\dot{\varepsilon}^p_{ij} \geq 0$. Here, $g = g(\sigma) \geq 0$ is the plastic potential function and $\dot{\lambda} > 0$ the plastic parameter.

If g is defined by the yield function f, the plastic flow rule is called associated flow rule and is defined by equation 2.4.

$$\dot{\varepsilon}^p_{ij} = \dot{\lambda} \frac{\partial f}{\partial \sigma_{ij}} \qquad (2.4)$$

By assuming the von Mises yield criterion 2.2, and utilising the plastic flow rule 2.4, the plastic strain rate can be explicitly stated as:

$$\dot{\varepsilon}^p_{ij} = \frac{3\dot{\lambda}}{2\sigma_{eq}}\left(\sigma_{ij} - \frac{1}{3}\sigma_{kk}\delta_{ij}\right) = \frac{3\dot{\lambda}}{2\sigma_{eq}}\sigma'_{ij} \qquad (2.5)$$

where δ_{ij} is the Kronecker delta and is defined by:

$$\delta_{ij} = \delta_{ji} = \left\{ \begin{array}{ccc} 1 & \text{if} & \text{i=j} \\ 0 & \text{if} & \text{i} \neq \text{j} \end{array} \right. \tag{2.6}$$

From the plastic strain rate, equation 2.5, it is evident that the plastic strain rate tensor is proportional to the stress deviator and is therefore also a deviatoric tensor. The plastic volumetric strain rate is zero, and as a result there is no volume change due to plastic deformations of the material, under the assumptions of a von Mises yield criterion.

2.1.3   Work hardening

When materials are plastically deformed, they usually work-harden which means that the stress carrying capacity increases. The two most common work-hardening rules are isotropic and kinematic hardening. Kinematic hardening accounts for translation of the yield surface in space, while isotropic hardening, which is used in this thesis, describes the growth of the yield surface. Isotropic work hardening was chosen due to the fact that no simulations were performed using cyclic loading. Thus, there is no need to incorporate a kinematic work hardening rule. For isotropic hardening, the elastic region expands while keeping the shape of the yield surface. When accounting for isotropic hardening, the hardening variable R is introduced, and the yield function becomes

$$f(\boldsymbol{\sigma}, R) = \varphi(\boldsymbol{\sigma}) - \sigma_Y(R) \leq 0 \tag{2.7}$$

$\sigma_Y = \sigma_0 + R$ is the flow stress and represents the strength of the material and σ_0 is the initial yield stress. The equivalent plastic strain p is determined from the plastic dissipation.

$$D_p = \sigma_{ij}\dot{\varepsilon}^p_{ij} = \sigma_{eq}\dot{p} \tag{2.8}$$

which makes $\dot{p} = \dot{\lambda}$ for the associated flow rule. The general form of the isotropic hardening rule is $\dot{R} = h_R\dot{\lambda}$, where the hardening modulus h_R depends on the state of the material. A rather common hardening law is the Power law, which is defined by equivalent plastic strain. The Power law was chosen as the hardening law in the numerical simulations performed in this thesis and is formulated as

$$R(p) = Kp^n, \tag{2.9}$$

where K and n are material parameters calibrated from the experimental data. When assuming an associated flow rule ($\dot{p} = \dot{\lambda}$), the hardening modulus becomes $h_R = Knp^{n-1}$.

2.2 Instability damage and fracture

Material fracture mechanics is about predicting the fracture behaviour from the material microstructure and material properties. The governing properties of ductile fracture and the GTN model will be presented.

2.2.1 Diffuse necking

To identify the material behaviour of the X65 steel, cylindrical uniaxial tension tests were conducted. Based on the force and diameter reduction in two directions, the true stress versus plastic logarithmic strain curve can be established by the equations below, where A is the area, D_x and D_y are diameters in x- and y-direction, and F is the force.

$$A = \frac{\pi D_x D_y}{4} \quad (2.10) \qquad \sigma_t = \frac{F}{A} \quad (2.11) \qquad \varepsilon_l = \ln\left(\frac{A_0}{A}\right) \quad (2.12)$$

For smaller values of the equivalent plastic strain, the plastic deformation is stable with a continuously rising external load. However, when experiencing larger plastic deformations, the specimen may either start to experience a deformation instability or simply fracture due to damage processes, whatever comes first. In the case of an instability, a local neck or shear band due to localisation of plastic deformations usually occurs. This is called diffuse necking and is a vital precursor to the final failure. When the deformations start to localise into a diffuse zone, the external load will begin to decrease. Thus, the onset of diffuse necking is defined by the equation $dF = 0$. Under the assumption of a constant material volume under plastic deformation, the incremental strain becomes

$$d\varepsilon_l = \frac{dl}{l} = -\frac{dA}{A} \tag{2.13}$$

and $dF = d(\sigma_t A) = d\sigma_t A + \sigma_t dA = 0$ gives

$$\frac{d\sigma_t}{\sigma_t} = -\frac{dA}{A} = d\varepsilon_l \tag{2.14}$$

which leads to the expression for diffuse necking in the following equation

$$\frac{d\sigma_t}{d\varepsilon_l} = \sigma_t \tag{2.15}$$

Another name for the diffuse necking criterion is the Considère criterion. It states that the straining of the specimen is uniform until the slope of the true stress versus logarithmic strain curve equals the true stress, or when the force reaches a maximum. Geometric softening now overtakes the work-hardening. After this point, all plastic deformation takes place inside the neck, and the rest of the gauge region unloads elastically. Figure 2.2 illustrates where necking occurs on the stress-strain curve.

2.2.2 Ductile damage

The three most common fracture mechanisms in metals are ductile fracture, cleavage and intergranular fracture (Anderson, 2005). In this thesis, the focus will be on ductile fracture, but it should be mentioned that when studying pipes for the transportation of CO_2 etc, the ductile-to-brittle behaviour transition is important. Therefore, the cleavage and intergranular fracture mechanisms will be important too and should be considered for future work. Ductile damage evolution and fracture in metallic materials occur by nucleation, growth and coalescence of microscopic voids that initiate at inclusions and second-phase articles. Figure 2.2 illustrates the behaviour of a tensile test when it reaches a maximum force at the instability point; diffuse necking occurs, and a neck starts to form. It also describes two alternative stress-strain paths after failure, depending on the percentage of second-phase particles in the material (Anderson, 2005).
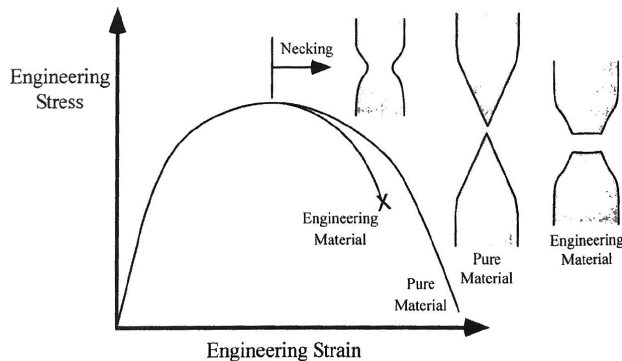

Figure 2.2: Uniaxial tensile behaviour in a ductile material where necking occurs, and two alternative failure paths after failure is illustrated. Figure from (Anderson, 2005).

Figure 2.3 explains the failure of ductile materials due to void nucleation, growth and coalescence. A void forms around an inclusion or second-phase particle in the material when the stress is sufficient enough to split the surface between the particle and the rest of the matrix. Once the void has been formed, further plastic strain of the matrix and hydrostatic stress contributes to the growth of the voids. Eventually, there will be localised plastic deformation and necking between the voids, and failure by void coalescence takes place. The fracture path orientation is dependent on the stress state. A cup and cone formation often occurs in uniaxial tensile specimens, because the necking results in a triaxial stress state in the specimen, with higher hydrostatic stress in the center of the specimen, which makes the voids coalesce in the center earlier than in the outer ring. This leaves the center region to have the typical dimpled surface which is common for ductile fracture, while the outer ring surface is more smooth as a result of a mainly shear dominant failure mode (Anderson, 2005).
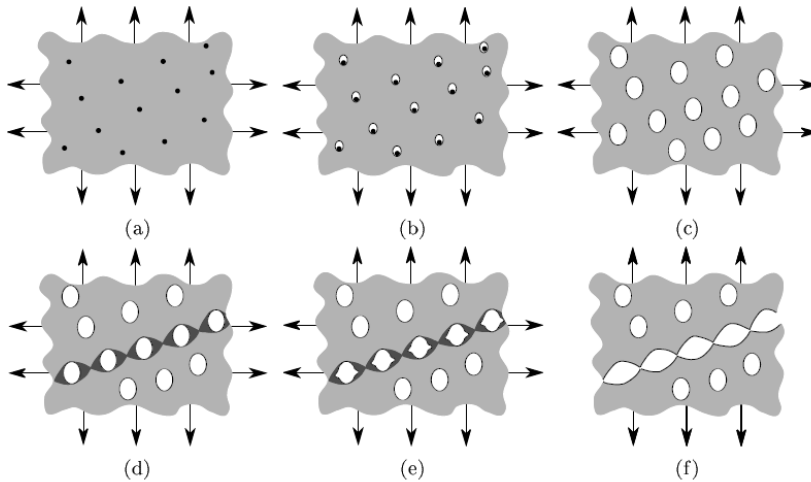
Figure 2.3: Illustration of void nucleation, growth and coalescence in ductile materials. Figure from (Anderson, 2005).

2.2.3 Porous plasticity

In an uncoupled damage model in simulations of large-scale structures, the damage variable has no coupling to the elastic-plastic response. Failure occurs at a critical damage variable. A coupled model, on the other hand, will take the interaction between the damage evolution and the plastic behaviour into account. Then, strain softening may occur if the damage evolution by void nucleation and growth outrun the work hardening in the rest of the matrix, and as a result, the strain will localise (Hopperstad and Børvik, 2017b).

One coupled model of porous plasticity is the GTN model, which is valid for isotropic porous metallic materials by assuming that the material behaves like a continuum. The Gurson model is based on micromechanics of voided materials. This means that it is valid for porous isotropic metals. The matrix material in the Gurson model is described by the von Mises yield criterion, whereas the inclusion of voids is the ingeniousity of the model. The Gurson model is thus able to describe the pressure sensitivity of porous materials, as well as describing the coupling of damage in a rather simple as well as a micro-mechanically based fashion. The voids described in the Gurson model will grow with increasing plastic strain, resulting in a steadily increasing void volume fraction. In this way, damage coupling is introduced in the form of void growth.

Gurson's model has later been modified by many authors, where the most well known were proposed by Tvergaard and Needleman. They introduced a hydrostatic stress dependence, and today the most used model is the Gurson-Tvergaard-Needleman (GTN) model and this will also be the one used in this thesis. Tvergaard and Needleman introduced the material constants q_1, q_2 and q_3 to obtain better description of material data obtained from experiments. The introduction of these material parameters was proposed mainly due to the discrepancies resulting from hardening of the matrix material. The original yield criterion proposed by Gurson (Gurson, 1977) was

$$f = \left(\frac{\sigma_{eq}^2}{\sigma_Y^2}\right) + 2qf_0\cosh\left(q\frac{\sigma_{kk}}{2\sigma_Y}\right) - (1 + qf_0^2) = 0 \tag{2.16}$$

where f_0 is the void volume fraction, $\sigma_{kk} = 3\sigma_H = \sigma_1 + \sigma_2 + \sigma_3$ where σ_h is the hydrostatic stress and σ_Y is the flow stress. The equivalent stress $\sigma_{eq} = \sigma_{VM}$ where σ_{VM} is the von Mises stress.

Tvergaard later modified the Gurson model in equation 2.16, giving a more detailed model of void growth (Tvergaard, 1982), (Tvergaard, 1981), which resulted in the GT model below

$$f = \left(\frac{\sigma_{eq}^2}{\sigma_Y^2}\right) + 2q_1 f_0\cosh\left(q_2\frac{\sigma_{kk}}{2\sigma_Y}\right) - (1 + q_3 f_0^2) = 0 \tag{2.17}$$

where the constants q_1, q_2 and q_3 typically have the values $q_1 = 1.5$, $q_2 = 1.0$ and $q_3 = q_1^2$.

Figure 2.4 illustrate how the stress carrying capacity is increasing when $f_0 \to 0$ and is decreasing as $f_0 \to 1$. When $f_0 = 0$, the material has no voids and is fully dense, resulting in a pressure insensitive material response. As seen from equation 2.17 and Figure 2.4, the GT yield criterion reduces to the von Mises yield criterion in equation 2.2 when $f_0 = 0$. When $f_0 = 1$ the material has no density and thus no load carrying capacity. As a result of this, the GT and the GTN model usually gives reasonable results for $f < 0.1$ (Abaqus, 2016). All the above is also the case for the GTN model in equation 2.18, where $f*$ is a modified version of the void volume fraction f_0.
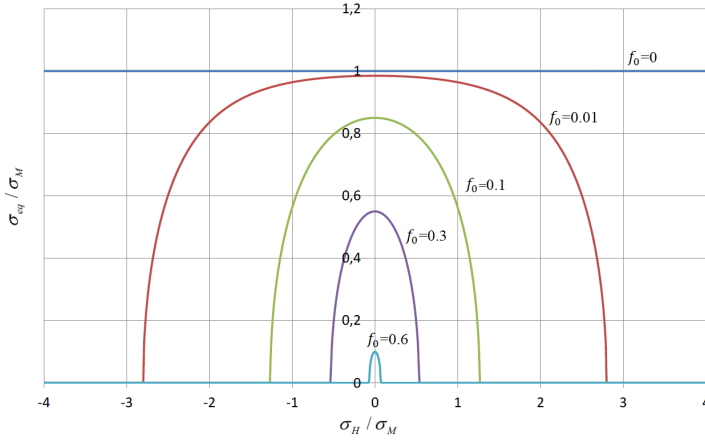

Figure 2.4: GT yield surface dependence on σ_{eq}/σ_M vs. σ_H/σ_M for different void volume fractions values f_0 by equation 2.17. $q_1 = 1.5$, $q_2 = 1.0$ and $q_3 = q_1^2$ and the figure is taken from (Hopperstad and Børvik, 2017b).

Tvergaard and Needleman modified the GT model by introducing a bi-linear function for the void volume fraction, through the variable f^* to account for the accelerated void

growth that occurs during void coalescence (Tvergaard and Needleman, 1984), and the
resulting GTN model is as follows:

$$f = \left(\frac{\sigma_{eq}^2}{\sigma_Y^2}\right) + 2q_1 f^* \cosh\left(q_2 \frac{\sigma_{kk}}{2\sigma_Y}\right) - (1 + q_3 f^{*2}) = 0 \qquad (2.18)$$

where

$$f^* = \begin{cases} f_0 & \text{if } f \leq f_c \\ f_c + \frac{\bar{f}_F - f_c}{f_F - f_c}(f_0 - f_c) & \text{if } f_c < f < f_F \\ \bar{f}_F & \text{if } f \geq f_F \end{cases} \quad \text{where } \bar{f}_F = \frac{q_1 + \sqrt{q_1^2 - q_3}}{q_3} \qquad (2.19)$$

Under the assumption that $q_3 = q_1^2$, $\bar{f}_F$ becomes $\frac{1}{q_1}$. It should be mentioned that f
in the yield function is not the same f as in equation 2.19. The void volume fraction f_0
corresponds to the initial porosity of unloaded and undamaged material. The critical void
volume fraction f_c is the porosity at the onset of void coalescence, where the increase
in the void growth rate kicks in. The factor f_F is the value of void volume fraction at
which there is a complete loss of stress carrying capacity in the material. The parameters
f_c and f_F can be derived from unit cell calculations or calibrated on the experimental
data from notched tensile tests (Nonn and Kalwa, 2013), while f_0 can be calibrated from
experimental data from smooth tensile tests.

Chapter 3

Material tests and simulations

In order to calibrate the material model, experimental results from the thesis of Gry Hellum (Hellum, 2017) were used. The material under consideration in this thesis was X65 steel, which is common for steel pipes typically transporting oil and gas (Oh et al., 2007). According to PM international suppliers (PMinternational, 2018), the material has an approximate chemical composition and material properties as seen in Table 3.1. The steel pipe that the tension test specimens were taken from was rolled to pipes from plates and welded longitudinally. Figure 3.1 shows that the specimens are extracted from the opposite side of the weld, which is the area exposed to the largest deformation during forming of the pipe. The longitudinal direction of the pipe and the specimens is the same. The material model can be divided into an elastic and a plastic part. The X65 high-strength steel was modelled with isotropic elasticity, and the plastic response of the material was modelled with a GTN model. An associated flow rule has been employed. The strain hardening of the material is described by the use of a power law. The elasticity parameters, as well as the plasticity parameters of the hardening model were taken directly from Hellum's thesis. The GTN yield criterion was found by inverse modelling. The calibration in total will be presented in the following sections.
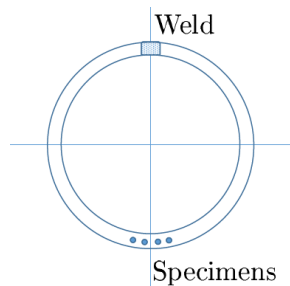

Figure 3.1: Pipe cross-section illustrating how the tensile specimens were extracted for experiments, figure taken from (Hellum, 2017).

3.1 Experimental study

In this section, the calibration of the elastic properties and the hardening model will be undergone. All the following up until section 3.2 was done by Hellum (Hellum, 2017), and is now to be explained for the reader.

Table 3.1: Information about the X65 steel composition.

Chemical composition							
C	Si	Mn	P	S	V	Nb	Ti
0.16	0.45	1.65	0.020	0.010	0.09	0.05	0.06

Yield strength	Tensile strength
Min. (KSI)	Min. (KSI)
65	77

3.1.1 Tensile tests

Quasi-static tensile tests at room temperature on four different specimens were conducted. The tests were done with a 100 kN Instron test machine with a velocity of 0.0025 mm/min. The test machine was screw-driven, and the load adjusts itself to the displacement to get a constant velocity. Two tests were done on each of the geometries, which are shown in Figure 3.2. The left side shows the geometry of the longitudinal side of the specimen, while the right side shows the cross-sections. The outer diameter was 5 mm, while the inner diameter in the gauge area was 3 mm. The four specimens in Figures 3.2a, 3.2b, 3.2c and 3.2d are from now on called Smooth, R2, R08 and V45 respectively. R2 and R08 had a notch with radius 2 mm and 0.8 mm respectively. For manufacturing reasons, an angle of 17.5° was made for the R08 specimen, as seen in Figure 3.2c. From Hellum's experiments in her thesis, R2 and R08 represent the higher values of triaxiality in the notched specimens, while the Smooth specimen represents a low triaxiality. The V45 specimen with an angle of 45° represents the highest triaxiality obtained from the experiments.
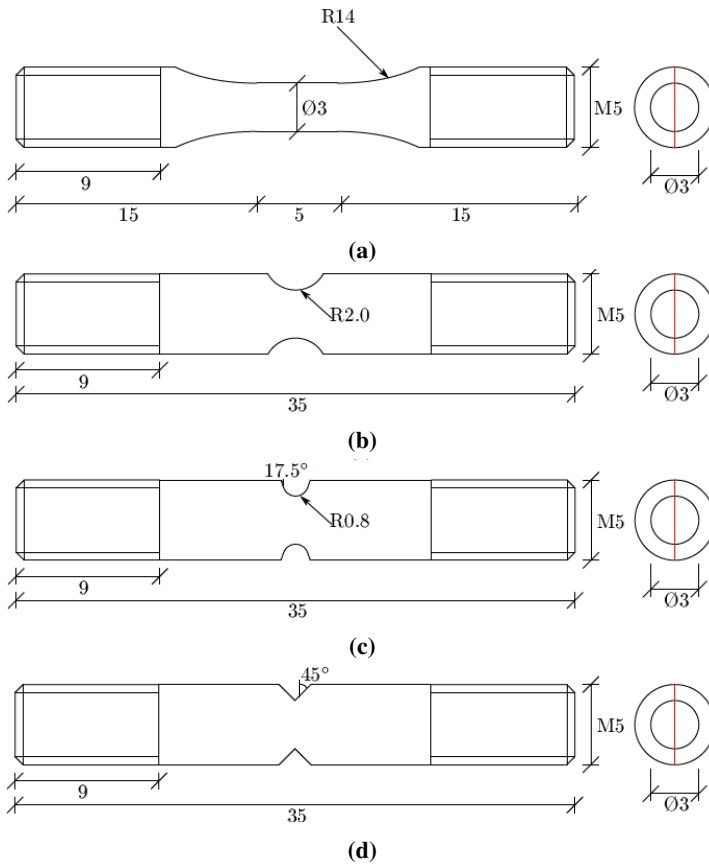
Figure 3.2: Geometry of tensile specimens **a)** Smooth, **b)** R2.0, **c)** R0.8 and **d)** V45. Figure from (Hellum 2017 p 41).

3.1.2 Results

Hellum used the smooth uniaxial tensile test to calibrate the hardening model. The force was measured by the Instron test machine, while the diameter reductions were found by lasers. Two tests were carried out on the same specimen geometry. The resulting data for force and diameter reductions were similar and made it acceptable to calibrate the material model to only one of the tests.

Hellum used the Bridgman (BLR) correction by equation 3.1, where a/R is described by LeRoy in equation 3.2 after necking. R is the notch radius, and a is the specimen radius in the neck.

$$\sigma_{eq} = \frac{\sigma_t}{(1 + 2R/a)\ln(1 + a/2R)} \tag{3.1}$$

$$a/R = 1.1(p - \epsilon_{lu}^p) \quad , \quad p > \epsilon_{lu}^p \tag{3.2}$$

Diffuse necking occurs at maximum force by Equation 3.3, as all plastic deformation now takes place inside the neck.

$$\frac{d\sigma_t}{d\epsilon_l} = \sigma_t \tag{3.3}$$

By using the BLR correction, Hellum was able to present the equivalent stress versus the plastic logarithmic strain. Hellum used least square fit to find the hardening model parameters, represented by Power law as already mentioned. The resulting parameters are presented in Table 3.2.

Table 3.2: Constants calibrated by Hellum (Hellum 2017 p 18,64).

Elasticity constants and density		
E [MPa]	ν	ρ [ton]
208E3	0.3	7.8E-9
Hardening model by Power Law		
A [MPa]	B [MPa]	n [-]
652.5	297.8	0.7281

When calibrating the hardening model from the Smooth test, Hellums material model described by Johnson-Cook hardening is spot on compared to the experimental data. When running the simulation on the Smooth specimen in Abaqus, the true stress versus logarithmic strain matches the experimental data for the yield stress and the slope of the curve in the beginning. When reaching higher strains, from 0.6 and upwards, the numerical model starts to overestimate the true stresses, as seen in Figure 3.3. The following sections will first present the finite element models for the four different tensile tests. Then, an additional part to the material model by Hellum will be introduced. The hardening model and the elastic parameters from Table 3.2 will be copied. The plastic flow will now be described by the GTN model, as this model may be able to represent the material behaviour more accurate at higher strains, by taking voids and void growth in the material into account. The density of the X65 steel will be represented by the void volume fraction f_0, which describes the presence of voids in the material.
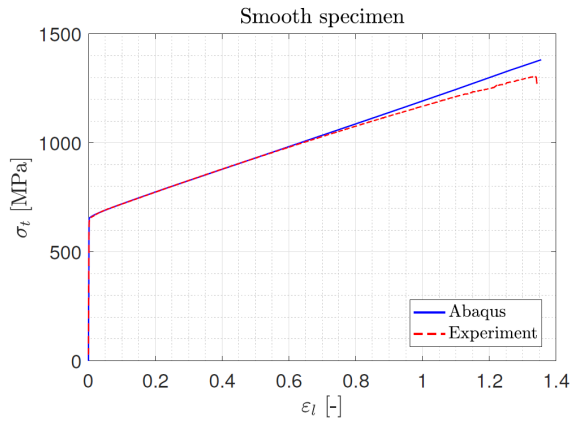
Figure 3.3: Experiment versus finite element model with Johnson-Cook material model, figure from (Hellum 2017 p 65).

3.2 Numerical study

In order to calibrate the GNT flow rule, numerical models for the four tensile tests were needed. As described in chapter 2, the values of the set GTN parameters were $q_1 = 1.5$, $q_2 = 1.0$ and $q_3 = q_1^2$. The constants f_0, f_c and f_F were then calibrated. Before calibrating the GTN parameters, two studies were performed to find an optimal velocity and a suitable mesh shape. For this, the GTN parameters were set to $f_0 = 0.002$, $f_c = 0.1$ and $f_F = 0.5$. The element type was also copied from Hellum, the 4-node bilinear axisymmetric quadrilateral with reduced integration and hourglass control, CAX4R.

3.2.1 Numerical models

Geometry

The parts were modelled as axisymmetric deformable shells in Abaqus. The geometry of the modelled specimens is shown in Figure 3.4, where 3.4a is Smooth, 3.4b is R08, 3.4b is R2 and 3.4d is V45.
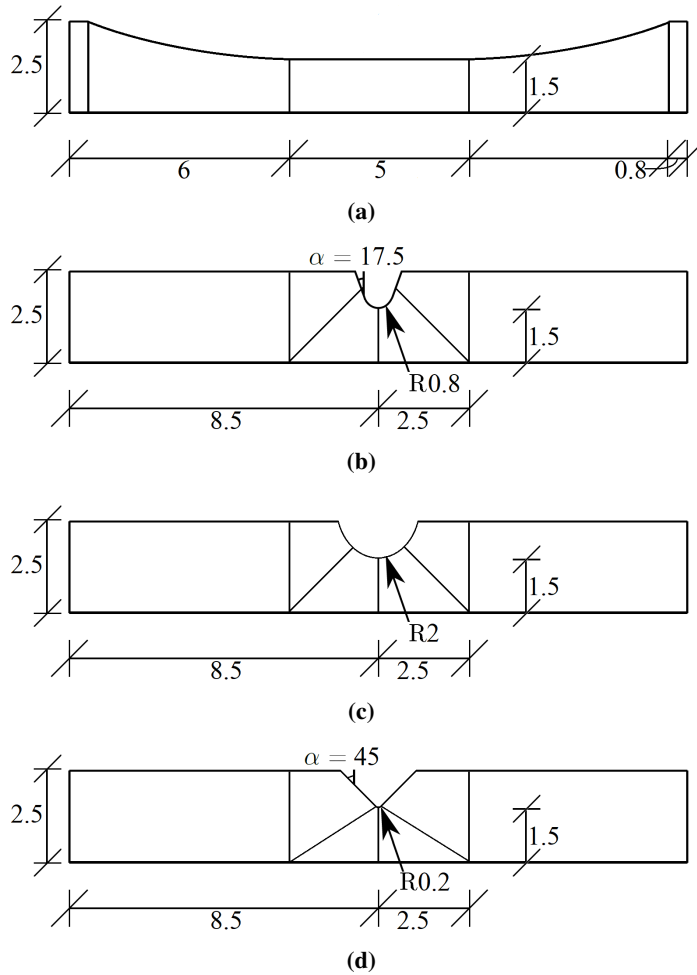
Figure 3.4: Geometry and partitioning of numerical models of tensile specimens **a)** Smooth, **b)** R08, **c)** R2 and **d)** V45.

Boundary conditions and loading

To simulate the experiments, the numerical models were fixed against movement in the longitudinal direction in one end, while a load was uniformly applied on the other end. The specimen was fixed against movement in the transverse direction along the line of axisymmetry. When implementing quasi-static behaviour in the dynamic explicit simulations, the analysis was sped up by time scaling since the material model was chosen to be rate-independent. For the sake of computational time, the time period should be as fast as possible without inertial forces becoming significant for the structure's response.
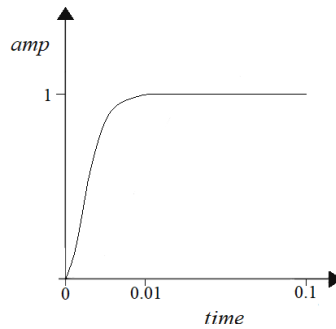
Figure 3.5: Illustration of the smooth step function in Abaqus.

For a quasi-static load case, the inertial forces are negligible due to small velocities. This makes the kinetic energy small, which can be used to validate that the simulation is in fact quasi-static. If the total time of the simulation were to be set too low, the kinetic energy could become significant compared to the internal energy, and the deformation would no longer be quasi-static. The value of the kinetic energy should not exceed 5% of the value of the internal energy throughout the process. If moving the plate instantaneously, a stress wave through the model could be induced, giving unwanted results. This was solved by ramping up the load by using a smooth step amplitude, as seen in Figure 3.5. The chosen amplitude was 10% of the time period (Abaqus, 2016).

Deformation velocity

Before a mesh study was performed, a suitable velocity was established for the Smooth model, where the mesh was identical to the one used by Hellum (Hellum 2017, p 20). When the velocity was increased, the presence of oscillations decreased, as Figure 3.6 shows, while the running time increased. The point of fracture was only slightly affected by the velocity, but since this behaviour was also to be adjusted by the constants f_c, f_0 and f_F, this did not need to be considered for now. In the analysis, both the viscous and frictional damping energy is zero. Therefore, the energy balance for the entire model can be shortened down to $E_I + E_{KE} - E_W = E_{TOTAL}$ where E_I is the internal energy (elastic and plastic strain energy), E_{KE} is the kinetic energy, E_W the work done by external forces and E_{TOTAL} the total energy in the system (Abaqus, 2016). The total energy of the system should remain constant for a stable analysis, and for a quasi-static analysis, the external forces are close to equal to the internal energy. The artificial strain energy includes energy stored in hourglass resistance and transverse shear in shell and beam elements. The artificial energy should be as low as possible as it represents an artificial stiffness in the model.
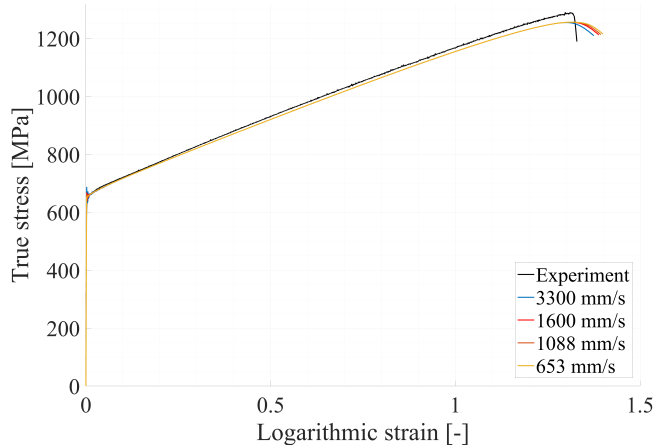
Figure 3.6: Effect of velocity change in gauge area of Smooth simulation, experiment versus simulations.

Table 3.3 shows the relation between internal and kinetic energy and the work done for the different velocities 3300 mm/s, 1600 mm/s, 1088 mm/s and 653 mm/s. When decreasing the velocity, the absolute value of the total energy decreased as expected. The total energy remained constant throughout the analysis for all the different velocities. The kinetic energy for all velocities was less than 1% of the internal energy. The artificial energy also remained less than 1% of the internal energy throughout the four analyses. However, only total kinetic energy was considered and may explain why there are still oscillations. Due to these oscillations, a step time of 0.002 seconds was chosen, as it gave a good representation of the data while keeping the running time low.

Table 3.3: Energy balance in simulations for the velocities 3300 mm/s, 1600 mm/s, 1088 mm/s and 653 mm/s.

Velocity [mm/s]	E_I [mJ]	E_{KE} [mJ]	E_W [mJ]	E_{TOTAL} [mJ]
3300	11008433.05	7057.81	11015512.90	-22.04
1600	10953346.42	1726.12	10955084.19	-11.65
1088	10955281.50	767.18	10956056.61	-7.93
653	10959059.87	276.34	10959340.87	-4.66

Mesh

The GTN model is highly mesh sensitive since the void growth eventually introduces strain softening, and so it was important to establish a suitable mesh size and shape before doing further studies on the parameters f_c, f_0 and f_F. The mesh size used by Hellum was considered to be a good solution, and so the mesh-study was mainly focused on finding the right element shape of the mesh. 28 elements over the thickness were used, while the

number of elements in the longitudinal direction was changed. Figure 3.7 illustrates the effect of changing the elements from square to oblong. The oblong elements were made so that l_x were larger than l_y, see Figure 3.8 for coordinate system. By doing so, they were less elongated in the longitudinal direction when stretched, keeping a better aspect ratio of the elements towards the end of the simulation. A correlation is seen between the shape of the elements and the shape of the curve, and only the shape of the elements in the area of fracture influenced the stress-strain behaviour. When changing the elements outside the zone of fracture, the stress-strain curve was not affected. As the mesh size is set by the zone of fracture, also called the process zone, this was to be expected when using the GTN model (Hopperstad and Børvik, 2017b). Therefore, the elements outside the gauge area were made large to positively affect the running time.
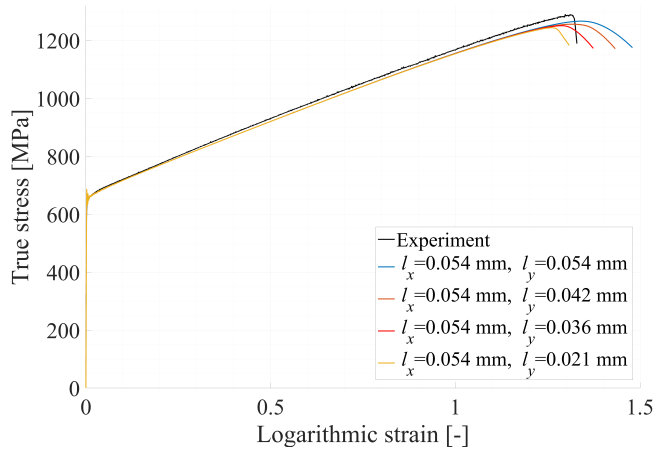

Figure 3.7: Effect of element shape in gauge area of Smooth simulation, experiment versus simulations.

The mesh $l_x = 0.054$ mm and $l_x = 0.036$ mm was chosen. As the stress-strain curve would be dependent on the parameters f_c, f_0 and f_F, it was difficult to know for certain whether or not the chosen mesh was the best. However, given the mesh-sensitivity of the GTN model, a mesh had to be established to be used in all later simulations. If the final stress-strain curve after calibrating f_c, f_0 and f_F matched, the mesh would be considered satisfying. Otherwise, it could be necessary to look at the element shape again.
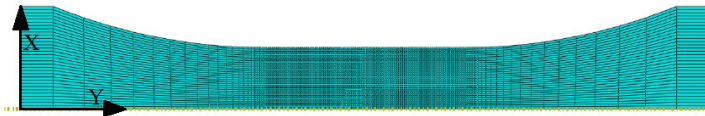

Figure 3.8: Illustration of the mesh used in the Smooth numerical model. The element lengths in the gauge area were $l_x = 0.054$ mm and $l_x = 0.036$ mm.

3.2.2 Calibration of Gurson–Tvergaard–Needleman

When calibrating the GTN parameters, the initial void volume fraction parameter f_0 was calibrated first. f_0 controls the shape of the true stress - logarithmic plastic strain curve, and was determined by inverse modelling on the Smooth tensile test in Abaqus. The parameters critical void volume fraction f_c and total void volume fraction f_F were then found. These parameters affects the material behaviour only at fracture. These were also found by inverse modelling, but by using the notched specimens. As one of the goals of this project were to be able to simulate a running crack, the critical parameters were originally mainly fitted to the sharp notch specimen V45, as the behaviour of the sharp notch were assumed the most similar to a running crack, and the Kahn-test described in chapter 4.

Initial void volume fraction

For the initial void volume fraction, simulations of the Smooth tensile test were run while changing only f_0 and keeping f_c and f_F constant at 0.1 and 0.5 respectively. Figure 3.9 shows the response for different values of f_0, and $f_0 = 0.00095$ was found to be the best fit.
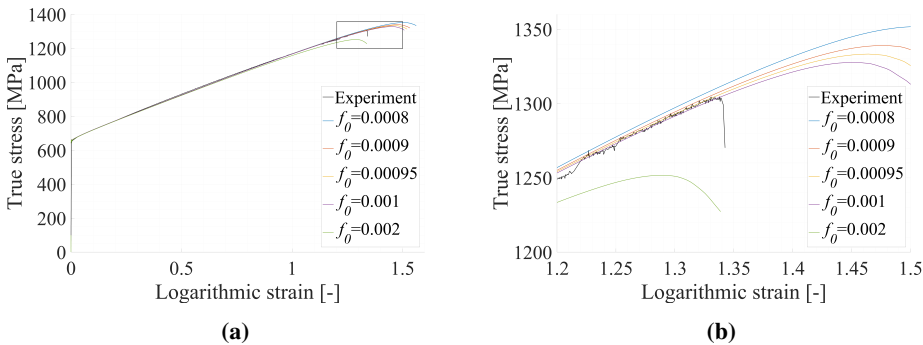

Figure 3.9: The effect of changing the void volume fraction f_0 in the numerical model of the Smooth simulation, compared to experimental data. Figure **b**) is the area in the black square in Figure **a**).

Critical and total void volume fraction

When changing f_c in the V45 simulations, f_F was kept constant at 0.3. Figure 3.10 shows that when increasing f_c, the true stress - plastic log strain curve converges and stabilises for higher values. What is also seen in Figure 3.11 is that the value of f_F only affects the shape of the curve after maximum true stress, affecting only the steepness of the curve at fracture. As this part is not of interest for the behaviour up until fracture, the parameter was set to 0.3. As for the critical void volume fraction f_c, increasing the value seemed to give better-looking curve, but neither of the parameters gave noteworthy results, so the parameters were tried fitted to the R2 and R08 notched tests as well.
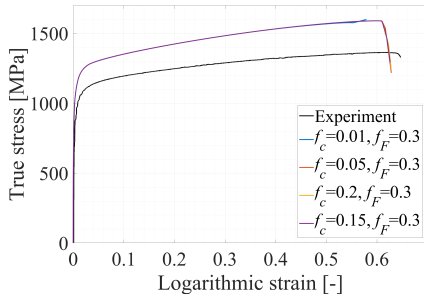
Figure 3.10: Results when changing f_c for V45 simulation, compared to experimental data.
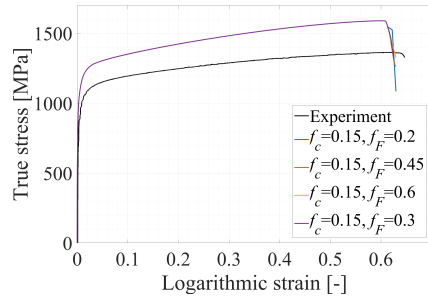

Figure 3.11: Results when changing f_F for V45 simulation, compared to experimental data.

As it was found from Hellum's results, the true stresses for the numerical simulations are too high compared to the experimental results. This will be investigated further in section 3.2.3. The inverse modelling and adjustment of the parameters were therefore mainly focused on matching the shape of the curve of the experimental results rather than matching these results completely.
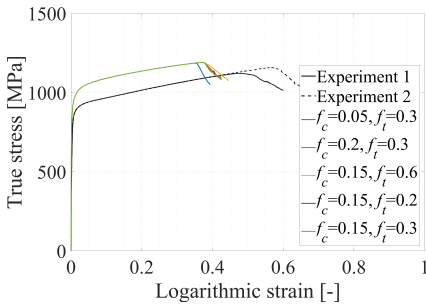
Notches R08 and R2

Figure 3.12: Effect of varying f_c and f_F for R08 simulation, compared to experimental data.
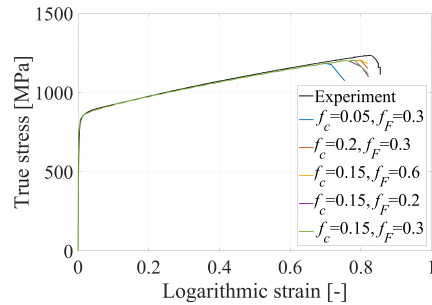

Figure 3.13: Effect of varying f_c and f_F for R2 simulation, compared to experimental data.

For the simulations done for the R08 notched and the R2 specimens, the true stresses were also too high, especially for the R08 notch, as seen in figure 3.12. The R2 notch with a larger diameter gave true stresses more similar to the experimental data. For all specimens however, the shape of the curve matched the experiments well, although some of the numerical simulations showed an earlier point of fracture. This was guessed to be because of the high stresses. Common for all of the specimens was that changing the values of f_c and f_F did not influence the true stress curves noteworthy, as Figures 3.10,3.11,3.12 and 3.13 shows. The stress levels and the point of failure were unchanged as long as $f_c >$ 0.1. Due to this, the values of $f_c = 0.15$ and $f_F = 0.3$ were chosen as the coalescence and fracture criterion values for the material model. This gives a resulting material model seen in table 3.4. The results of the simulations using these material parameters together with the experimental data are seen in Figure 3.14.
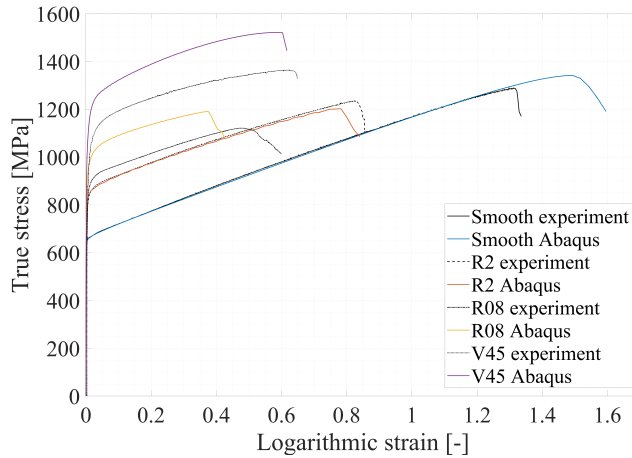
Figure 3.14: Final numerical results for Smooth, R08, R2 and V45 simulations with the chosen GTN parameters described in Table 3.4, compared to experimental data.

Table 3.4: Final GTN model.

Elasticity constants and density		
E [MPa]	ν	ρ [ton]
208E3	0.3	7.8E-9
Work hardening by power law		
A [MPa]	B [MPa]	n [-]
652.5	297.8	0.7281
GTN yield function material parameters		
q_1	q_2	q_3
1.5	1	2.25
GTN yield function failure criterion		
f_0	f_c	f_F
0.00095	0.15	0.3
l_x [mm]	l_y [mm]	l_z [mm]
0.036	0.054	0.054

3.2.3   Troubleshooting & improved numerical models

In an attempt to find out why the stress levels for the numerical simulations were too high when the notch radius got smaller, different techniques by trial and error were carried out. A first thought was pressure sensitivity of the material, something known for steel, and that our chosen material model was not able to capture the effect due to hydrostatic pressure on the notch. To try to account for this, analyses were run using the Drucker-Prager material model.

Another theory for the results was that there was something wrong with the experimental data or the calibration. Four new experiments were carried out, one test for each specimen. The specimens were from the same batch as the ones Hellum used, and diameter reduction was measured using Digital Image Correlation in eCorr, while Hellum used lasers. The GTN model was calibrated again from the force-diameter reduction.

The q-parameters used in the GTN model were also tried changed, as the original parameters were not initially fitted to the model, but found to be the correct ones from literature.

At last, the geometry of the numerical model was changed slightly, changing the radius of the specimens and making small alterations in the existing geometries.

Drucker-Prager

A disadvantage of the GTN model is that is assumed independent of the hydrostatic pressure (Hopperstad and Børvik, 2017a). Therefore, to check the effects of hydrostatic pressure in the model, tests were run using the Drucker-Prager yield criterion. The Drucker-Prager model is an isotropic and pressure dependent model, where the deviatoric strength increases with increasing pressure (Holmen et al., 2017). In Abaqus, the linear Drucker-Prager criterion is written as (ref Abaqus):

$$f = t - p\tan\beta - d = 0 \qquad (3.4)$$

Where β is usually referred to as the friction angle of the material and controls the pressure sensitivity of the material. t is given by equation 3.5, where K is the ratio of triaxial yield stress in tension vs compression. The variable d represents the cohesion of the material and is given for uniaxial tension in equation 3.6.

$$t = \frac{1}{2}q[1 + \frac{1}{K} - (1 - \frac{1}{K})(\frac{r}{q})^3] \quad (3.5) \qquad\qquad d = (\frac{1}{K} + \frac{1}{3}\tan\beta)\sigma_t \qquad (3.6)$$

A flow potential G, is also defined for the linear Drucker-Prager criterion. This is given as:

$$G = t - p\tan\psi, \qquad (3.7)$$

where ψ represents the dilation angle in the p-t plane. In Abaqus, a linear model of Drucker-Prager was used, and inputs for this were the three parameters β, K and ψ. For this case, it was desired to use an isotropic and volume-conserving version of the Drucker-Prager criterion, and this was done by setting the flow stress ratio K to 1.0 and the dilation angle ψ to zero (Holmen et al., 2017). A hardening criterion for tension was also added to the model, using the values for plastic strain found by Hellum and seen in Table 3.2. As the use of Drucker-Prager was only done to check pressure sensitivity, only the parameter β was initially changed in the numerical simulations to simplify the model.

The friction angle β can be determined from uniaxial tension and compression tests as:

$$\beta = \tan^{-1}\left(3\frac{|\overline{\sigma_c}| - |\overline{\sigma_t}|}{|\overline{\sigma_c}| + |\overline{\sigma_t}|}\right), \qquad (3.8)$$

where $|\overline{\sigma_c}|$ is the stress in uniaxial compression, and $|\overline{\sigma_t}|$ is the stress in uniaxial tension. In this case, only the stress in uniaxial tension was known, and a pressure coefficient α was used instead to find β using equation 3.9:

$$\alpha = \frac{\tan\beta}{(3 + \tan\beta)} \leftrightarrow \beta = \tan^{-1}\left(\frac{3\alpha\overline{\sigma_t}}{1 - \alpha\overline{\sigma_t}}\right) \tag{3.9}$$

From Spitzig and Richmond (Spitzig and Richmond, 1984), α for different types of steel seemed to be laying at a value around 20, and based on this a value of β was found to be 2.3, given the yield stress previously found by Hellum to be 652.5 MPa.
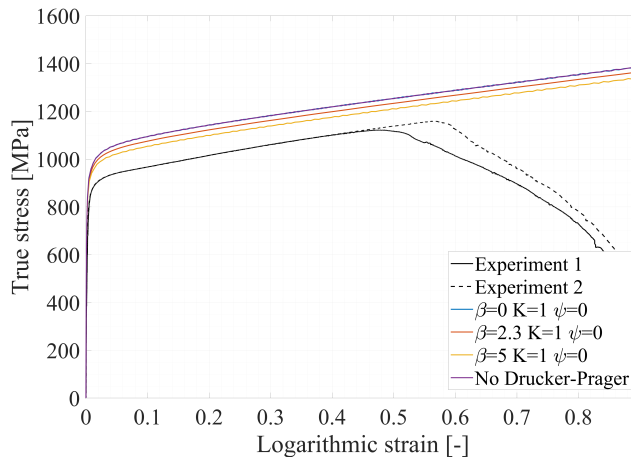

Figure 3.15: True stress vs logarithmic strain for R08 simulation varying the Drucker-Prager parameters, compared to experimental data.

As seen in Figure 3.15, a β value of 2.3 had little effect on the stress-strain curve, proving that the high difference between the numerical model and experimental results were not due to hydrostatic pressure sensitivity. A parameter study of the β value was also done to check the effects of the friction angle in Abaqus, as seen in Fig.3.15. It was found that a higher friction angle leads to lower stress-levels in Abaqus and less pressure sensitivity. Still, a β of 5, close to the pressure coefficient for aluminium 6070-T6 (Holmen et al., 2017) was still not enough to lower the stress levels to match the experimental data. The model in Abaqus was also run changing dilation angle ψ and triaxial stress ratio K, but these changes did not improve the results, and further studies on these parameters were not pursued.

New material experiments

In her thesis, Hellum did not use edge-tracing to measure diameter reduction on the tensile-tests, but rather lasers. Due to the deviation in the numerical results, a validation of the experimental results from Hellum was desired. Four tensile tests, one smooth and three notched specimens from the same batch as Hellum were performed, but this time using

high-resolution cameras to be able to perform edge-tracing on the edges to measure diameter reduction. An Instron machine with a 100 kN load cell, similar to the original experiments was used, with a velocity of 0.15 mm/min. The edge-tracing was performed by Egil Fagerholt using the software eCorr, measuring the diameter from two different angles, and the force was measured by the Instron machine. The results were then processed in Matlab to get stress-strain curves for the four tests. The results are presented together with the original experiments in Figure 3.16.
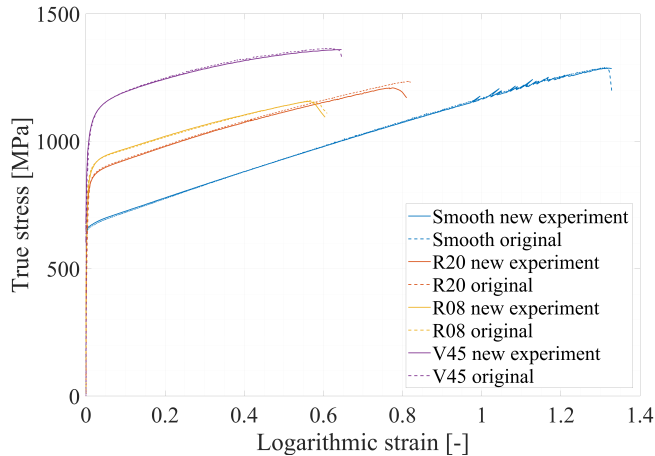
Figure 3.16: Experimental results from old versus new experiments conducted for Smooth, R08, R2 and V45.

These results verify the experimental results from Hellum, as all of the curves from the four tests are coincident with each other. A calibration of the elastic properties and the hardening law was also conducted from the experimental results, to verify the parameters used by Hellum. The recalibration gave the same results as Hellum, given in Table 3.3.

Parameter and geometry studies

- In the previous models run using the GTN model, the material parameters q_1, q_2 and q_3 were set to the standard set by Tveergard (Tvergaard, 1982). To find out if the value of q could have any effect on the results, a simulation of the V45 specimen was run putting $q_1 = q_2 = q_3 = 1$. The results are seen in Figure 3.17. When using Gurson's original model where $q_1 = q_2 = q_3 = 1$, but then the coalescence and fracture criterion was removed (Gurson, 1977), this gave the same results as $q_1 = q_2 = q_3 = 1$. As changing the material parameters did not affect the yield point of the curve, a further analysis of the values of q_1, q_2 and q_3 was not done.
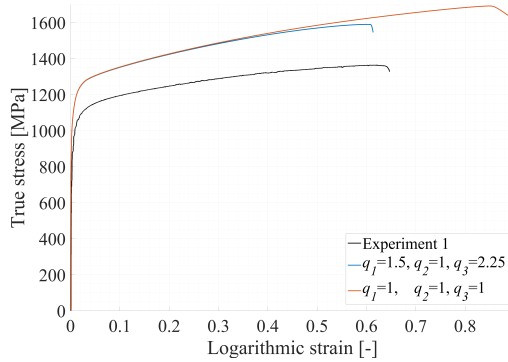
Figure 3.17: Effect of changing the material parameters q_1, q_2 and q_3 on V45 simulation, compared to experimental data.

- As the V45 specimen was supposed to be sharp, but still has a notch of 0.2 mm, the radius of the notch was tried changed. When changing the radius to 0.1 mm and 0.3 mm, the magnitude of the stresses was not dramatically changed, as shown in Figure 3.18. When the radius was made smaller, the stress magnitude was decreased, but the results were still not satisfactory. There was no point in making the radius smaller, as this was not possible due to machining.
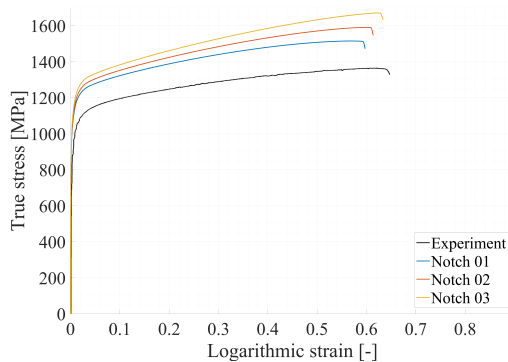

Figure 3.18: Effect of varying the notch radius on V45 simulation, from 0.1 mm to 0.3 mm, compared to experimental data.

- Since changing the radius in the V45 specimen did not give helpful results, the geometry needed to be investigated further. Therefore, the geometry of the R08 specimen was studied. When investigating some undeformed specimens, it looked like the bottom of the notch was more flat, and not completely circular. Therefore, the geometry was changed, so that the bottom of the notch was flattened out. Not completely flat, but with a tiny curving to make the specimen fail in the middle, like the experiments. It showed that introducing even a very small flat area in the notch

had a huge effect on the stress-strain curve. Given the small size of the specimens used in the test, and the apparent deviation in results for small changes in the geometry for the R08 notch, it was decided to run a proper analysis to find the exact geometry of the specimens used in these tests.

Edge-tracing

Using the pictures from the new test performed in section 3.2.3, a Python script was developed by Sondre Bergo (personal communication, 13.03.18), with the purpose of edge-tracing the pictures in order to get the notch geometry as exact as possible (Appendix 1). This was done for the specimens V45 and R08, and the results were imported into Abaqus, creating a 2D axisymmetric model of the specimens in Abaqus. The same conditions as the previous numerical models were then applied and simulations were run.

The results were rather extraordinary. After running the first R08 test, the stress-strain curve seemed to follow the experimental curve almost precisely, and accounting for Drucker-Prager as well put the curve even closer to the original experimental results, as seen in Figure 3.19. The same was seen for the V45 test, the resulting true stress-strain curve was a lot closer, as seen in Figure 3.20. An edge-tracing analysis was also done on the R2 specimens, giving little improvement to the results. This was expected as the R2 original simulations fit the true stress-strain curve quite well, and the large diameter of the specimens was easier to machine. No edge-tracing was done on the Smooth specimen.
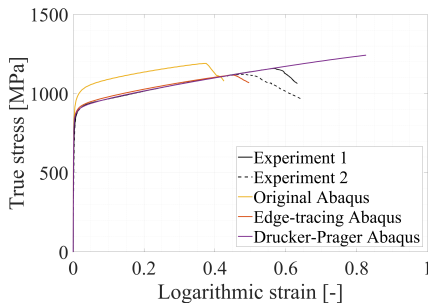

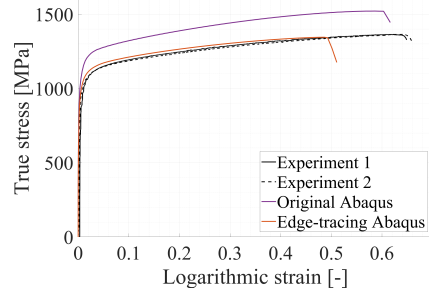**Figure 3.19:** Numerical results for R08 with edge-tracing, compared to experimental data.

Figure 3.20: Numerical results for V45 notch with edge-tracing, compared to experimental data.

The results from the geometry studies were rather surprising and proved that the geometry of the specimens was more important than previously thought. The results were extremely sensitive to the geometry of the notch. For specimens of the size in these experiments, a small imperfection will have more effect on the results than a crack of similar size on a larger specimen. The machining is therefore especially important for specimens of this scale.

Another factor to consider for such small samples is the possible presence of inhomogeneities. The risk of inhomogeneity is with few exceptions present in any material (Pauwels et al., 1998), and for such small tests, inhomogeneities will have a more signifi-

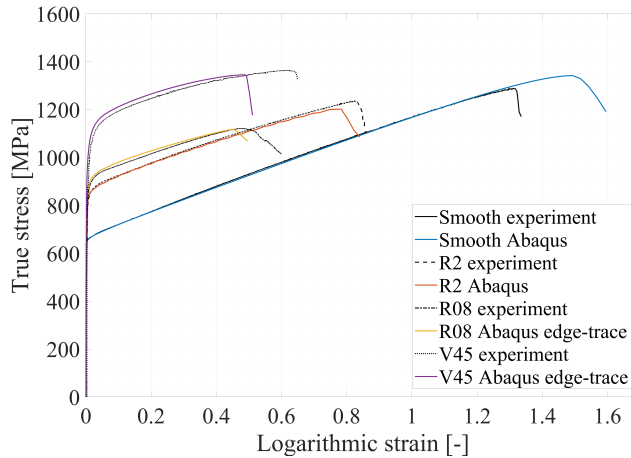cant effect on the material response, than tests on larger specimens.

Figure 3.21: Final numerical results for Smooth, R08, R2 and V45 simulations with the chosen GTN parameters described in Table 3.4, after improving the geometry of R08 and V45 using edge-tracing, compared to experimental data.

3.2.4 Evaluation of results

After getting the exact geometry of the tensile test, the GTN parameters found in this chapter proved to be able to represent the experimental results quite well, as seen in Figure3.21. However, the geometry of the specimens and precise machining proved to be way more important than previously thought, and for further studies, this is something that needs to be considered when calibrating material models from small specimens.

Of the GTN parameters calibrated, the initial void volume fraction f_0 was found to be the most influential for the results. The critical and total void volume fraction were found to have little effect on the stress-strain curves for this study, but further analyses could be done using the new geometry found in edge-tracing to investigate these parameters further. This may be important as previous studies by (Nonn and Kalwa, 2013) found that the most relevant parameters with regards to the GTN model were the volume fraction of secondary voids f_F, and element size.

The GTN model also proved to be highly mesh-sensitive, and for the notched specimens, it was impossible to recreate the exact dimensions of the element shape used in the smooth calibrations at the notch bottom. This was due to the geometry of the notch, and this could be the reason the failure occurs earlier in the numerical model for the notched specimens. For further use of the calibrated GTN parameters, the mesh geometry and shape in the zone of fracture should be as close as possible to the mesh found in this chapter for the best possible results.

Chapter 4

Tearing tests and simulations

To validate the GTN parameters found in chapter 3, Kahn tearing tests were performed using specimens taken from the same steel pipe as the four tensile tests, where the crack direction of the specimens represents the crack direction of the pipe. Using Digital Image Correlation (DIC), a force-elongation curve for the experiments was found. An X-ray Computed Tomography (CT) scan of the specimens after the tests was also carried out. A numerical model was then established and compared to the experimental results. The crack tunnelling was also studied using the CT scans of the Kahn test and the numerical model.

The Kahn tearing test follows the same principle as the DWT, explained in the literature study. This tearing test was conducted by Völling et al. and it was found that the DWT specimens and a pipe had similar stress-strain conditions and that the direct transferability of the parameters between the DWT model and a pipe was valid (Dr Alexander Völling, 2013). The DWT was also used by Scheider et al. (Scheider et al., 2014) and Nonn & Kalwa (Nonn and Kalwa, 2013) because of the results found by Völling et al.. Because of this, it is reasonable to assume a transferability between the Kahn tearing test and a pipe also.
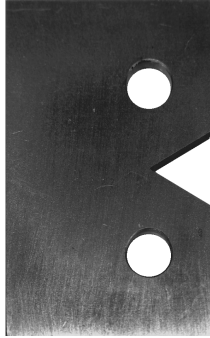
4.1 Experimental study
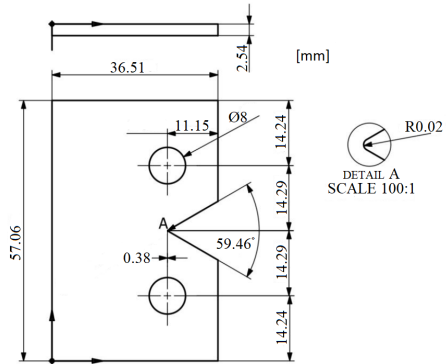

Figure 4.1: Picture of the Kahn specimen.

Figure 4.2: Dimensions of the Kahn specimen.

The Kahn tests were performed using a 250 kN Instron test machine. The specimens had dimensions as seen in Figure 4.2, and a specimen is seen in Figure 4.1. The radius of the neck was approximately 0.02 mm, but a variation of $\pm$ 0.01 mm might occur. Before running each test, each of the specimens were painted with a speckle-pattern, using white spray paint and black paint applied with an airbrush. This was done so that the DIC analysis performed after would be able to track the material deformation. Two high-resolution cameras were set up at each side of the machine perpendicular to the specimen, and during the tests, pictures were taken with a frequency of 1 Hz. All of the tests were run at a velocity of 1 mm/min. Force and displacement were measured continuously during the tests, and each of the tests were run until a different load after necking. In total five Kahn tests were performed, and the tests were stopped at respectively 2, 1, 15, 10 and 5 kN after necking. The set up of the tests can be seen in Figures 4.3 and 4.4.
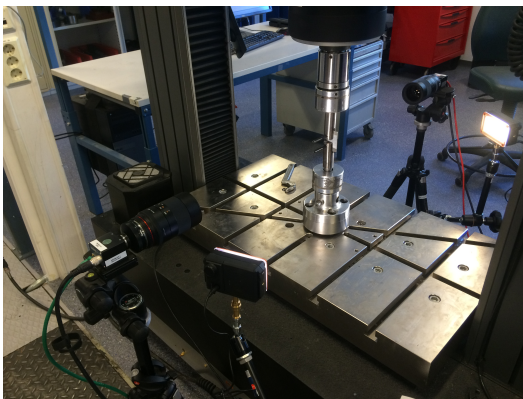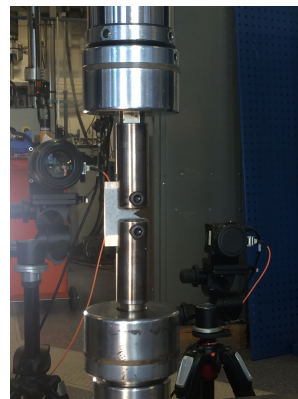

Figure 4.3: Set-up of Kahn text.

Figure 4.4: Set-up of Kahn test.

4.1.1 DIC - Digital Image Correlation

As the crosshead displacement of the Instron machine could be affected by the machine stiffness and give unprecise results, the displacement measured during the tests was not used for comparisons with the numerical model. Instead, the force was used together with vector elongation found from a Digital Image Correlation Analysis (DIC). To perform the DIC analysis, the pictures taken during the tests were analysed using the software eCorr.

The first step in the DIC analysis was to apply the mesh. A mesh of Q4 elements was applied to the first picture obtained before any displacement. The elements used in the mesh had a 20*20 pixel size, and the mesh was applied so that it followed the shape of the specimen in the zone of the predicted crack-path as seen in Figure 4.5. An analysis was then run for each test, applying gray value normalisation as well as element erosion for high strains over 1.2. This turned out quite well when using the camera with the highest resolution, Camera 1, but for the other camera, Camera 2, these settings made it difficult to run an analysis due to small lighting changes and instabilities in the pictures. After some troubleshooting, it was found that removing the gray value normalisation and applying two multilayers with 100 and 70 Q4 elements worked for the other camera.

The element erosion applied during the analysis was necessary as DIC only works as long as fracture has not occurred, so elements over the fracture surface were deleted during the analysis. Without element erosion, the elements that crossed the crack-path would get distorted. An appropriate element strain was found to be 1.2.
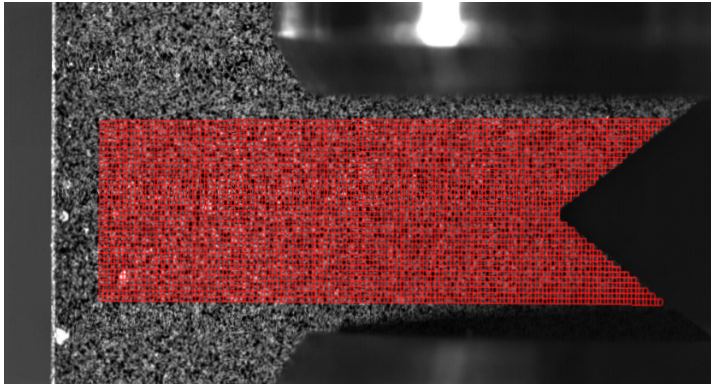

Figure 4.5: Illustration of the mesh used i eCorr for DIC.

After the analysis was done, a field map was applied to show element strain for each picture taken during the test, as seen in Figure 4.6. The effective principal strain, ϵ_{eff}, was the chosen field map in eCorr. This is based on the von Mises norm (eCorr, 2018) as:

$$\varepsilon_{eff} = \sqrt{\frac{2}{3}(\varepsilon_1^2 + \varepsilon_2^2 + \varepsilon_3^2)} \tag{4.1}$$

where ϵ_1 and ϵ_2 are the two in-plane principal strain of the two-dimensional Q4 elements of the mesh. The third principal strain component ϵ_3 (i.e., the through-thickness strain) can also be found in eCorr but is only valid where negligible elastic strains and plastic

incompressibility can be assumed (eCorr, 2018). ϵ_3 is found from conservation of volume to be:

$$\varepsilon_3 = -(\varepsilon_1 + \varepsilon_2) \tag{4.2}$$

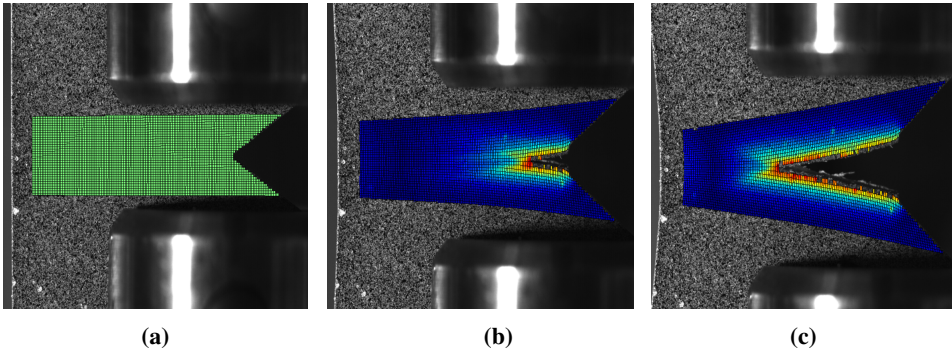
(a)   **(b)**   **(c)**

Figure 4.6: Field maps of effective strain for different stages of the Kahn-test.

The vector elongation used for the force-elongation curve was found by specifying a vector over the notch of the specimen of a given length and then exporting the vector elongation (vElong) for every picture. The vector was defined perpendicular to the crack-tip, and the length of the vector was the same as the vector used in the numerical Abaqus model, which will be explained in section 4.2.1. This was ensured using the ruler function in eCorr to measure pixels over a known distance and then translating this to mm. A shorter vector was also defined and compared to a similar one in the numerical model, proving that the vector elongation was dependent of the vector length and that both vector lengths corresponded to the numerical model. Therefore only the first vector length, as seen in Figure 4.7, was used for further studies.
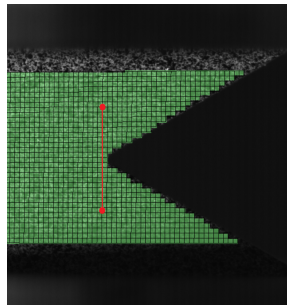

Figure 4.7: Vector used in eCorr.

Analyses for the vector elongation were run for all tests, but only the results for test 2,3,4 and 5 are presented in Figure 4.8, as the first test was run with a different speckle

pattern and cameras and required different settings. The force-elongation curve shows that the results follow each other with slight variations. The tests were stopped at different forces in the experiments for the CT scan in the following section, and the figure shows Kahn test 3 stopping at 15 kN, Kahn test 4 at 10 kN, Kahn test 5 at 5 kN and Kahn test 2 at 1 kN. The behaviour of the curve is similar for all tests, and therefore only the result from Kahn test 2 is used for later comparisons with the numerical model.
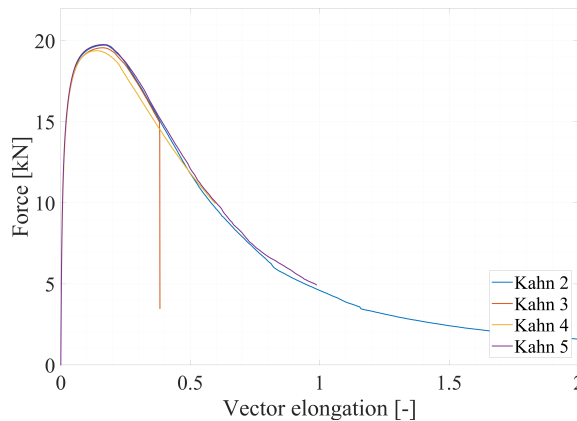

Figure 4.8: Force-elongation curves for the four different Kahn-tests.

The DIC analysis was done from two sides to get a better idea of the behaviour of the fracture. In Figure 4.9, the strain measured from both cameras for Kahn tests 2-5 are seen. As the figure shows, the strains for the two different sides are not identical, but they follow each other closely, indicating that the tearing test reacts similarly on both sides.
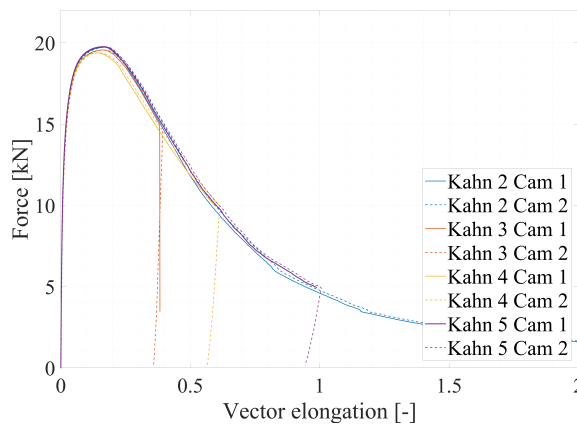

Figure 4.9: Force-elongation curve for the four Kahn tests measured from both sides, using pictures from Camera 1 and Camera 2.

4.1.2 X-ray computed tomography (CT) study

After performing the Kahn tests, the specimens were sent to for CT scanning at the Physics Department at NTNU. This was to get a better idea of how the fracture occurred, and especially to study the phenomenon of tunnelling in the specimens due to the triaxiality. According to Mathur et al. (Mathur et al., 1996), crack growth occurs by tunnelling in the central part of the plate and shear lip formation at the free surface. Tunnelling in crack growth refers to the situation in crack-growth through-thickness where the crack front grows faster in the center section of the specimen than closer to the specimen surfaces (Lan et al., 2010). This is a phenomenon much observed in ductile fracture experiments on specimens made of steel, and is due to the fact that the fracture criterion is first satisfied in the middle of the crack-front. A likely cause for this is that the specimen's center section is subjected to a state of high stress triaxiality. This promotes void nucleation, growth and coalescence, leading to crack growth. The GTN model is known to be a good model to explain this, and has been shown to be effective in predictions of crack growth in both two-dimensional plane strain conditions and three dimensional conditions, predicting that the crack will grow first in sections near the center of the specimens due to high triaxiality (Zuo et al., 2004). The results from the CT scan will therefore be compared to the numerical results using GTN in section 4.2.4.

As is seen in the Figures 4.10 - 4.13, crack tunnelling can be observed for Kahn tests 2-5. Kahn test 1 has not been studied. The red line in the left photos represents the location of the cross-section seen in the right photos. The photos show that voids exist in the centre of the section while the side surfaces have yet to fracture.

(a) (b)

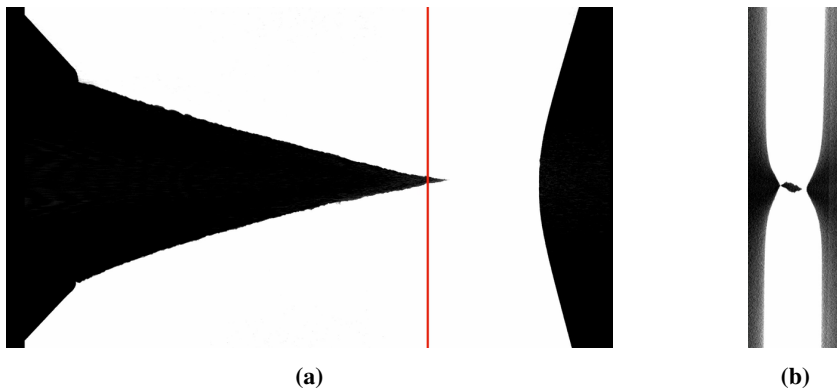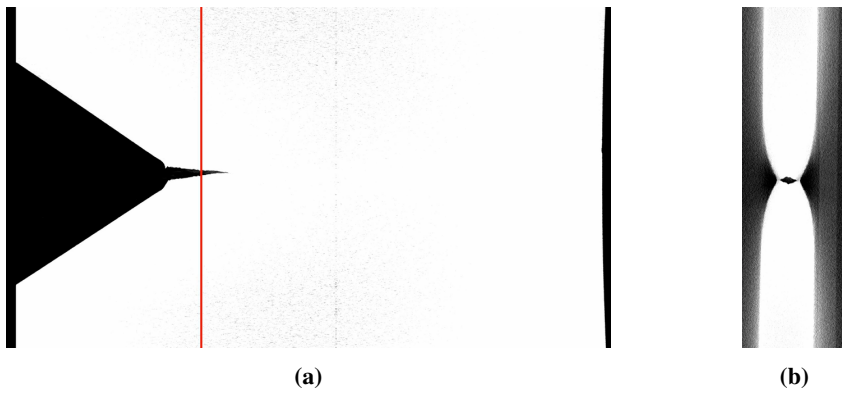**Figure 4.10: a)** Side view and **b)** cross-section of Kahn 2 CT scan.

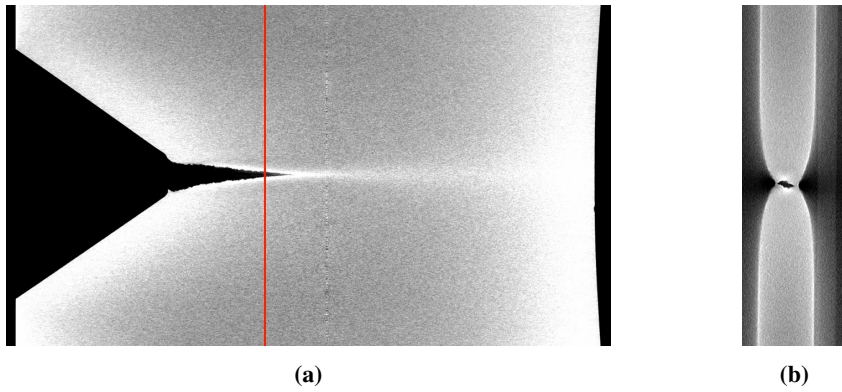Figure 4.11: a) Side view and b) cross-section of Kahn 3 CT scan.

Figure 4.12: a) Side view and b) cross-section of Kahn 4 CT scan.
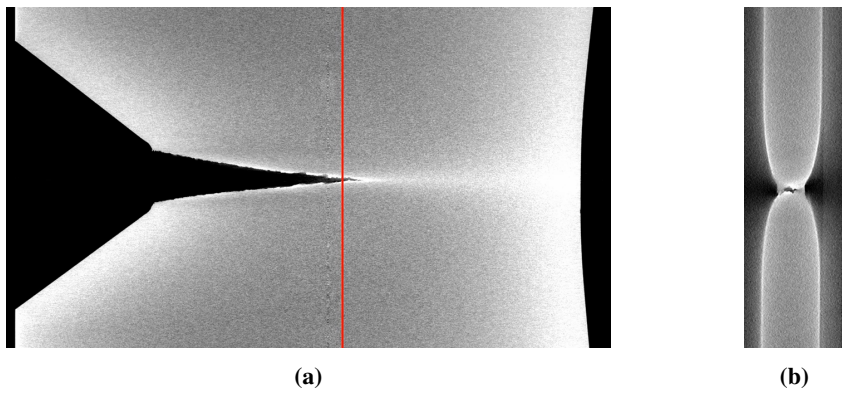

Figure 4.13: a) Side view and b) cross-section of Kahn 5 CT scan.

Figure 4.14 shows Kahn tests 2-5 a short time before the side surfaces close in the tests. The fracture behaviour varies a bit, where Kahn test 3 and 4 show a cup fracture, and Kahn test 5 a more slant fracture. Kahn test 2 is something in between. From experiments done by Zuo et al. (Zuo et al., 2004) in regards to tunnelling, both flat and slant crack-growth can be observed in stable tearing tests, and this seems to be the case in this study also. The behaviour of the crack may also be dependent on the length of the crack, as a more slant fracture is observed for the specimens with the longest crack. This is also observed by Zuo et al. (Zuo et al., 2004). The relation between tunnelling and the length of the crack will be explained further in section 4.2.4 .

(a)   (b)   (c)   (d)
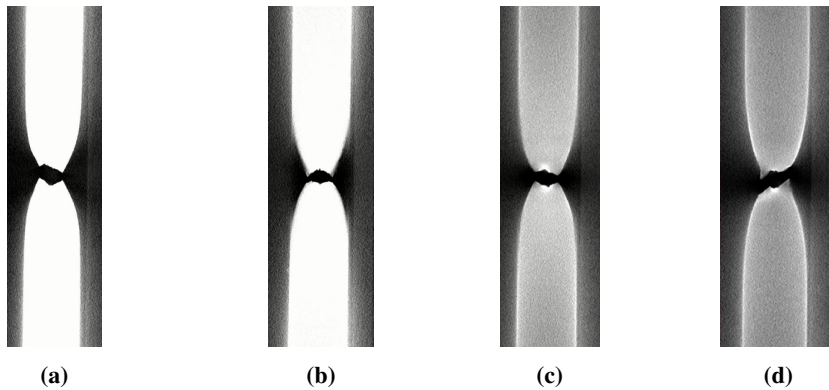
Figure 4.14: Cross-section of **a)** Kahn test 2 **b)** Kahn test 3 **c)** Kahn test 4 and **d)** Kahn test 5 during the CT scan.

Another interesting phenomenon observed for the second Kahn test, the test with the largest final crack length, is that an increasing thickness could be observed over the end of the crack-path. This is seen in Figure 4.15.

(a)   (b)

Figure 4.15: a) Side view and **b)** cross-section of Kahn 2 CT scan at the end of the experiment.

4.2 Numerical study

4.2.1 Numerical model

The Kahn tearing test was modelled in Abaqus with the dimensions as shown in Figure 4.2, while the material properties are given in Table 3.4. The Kahn specimen was modelled using 8-node linear brick elements with reduced integration, C3D8R. The simulations were run using the explicit solver, where the velocity was increased to 1500 mm/s to save computational ti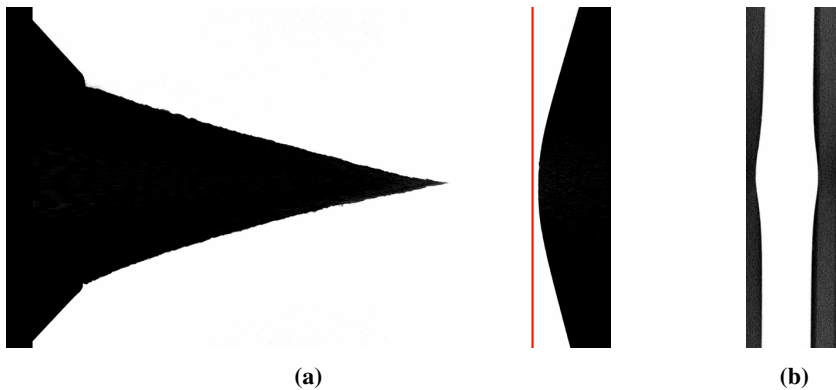me. The velocity of the analysis was first optimised so that in combination with ramping up the load by a smooth step as shown in Figure 3.5, the dynamic effects were negligible. A constraint of type kinematic coupling in the bolt holes was used to simulate the bolts of the 250 kN Instron test machine, inspired by the thesis by Sævareid (2017). The load was applied in Y-direction at the centre of the coupling, see Figure 4.16 for coordinate system. The coupling was fixed in all other directions except in radial direction, to ensure that the part was allowed to rotate around the Z-axis.

To decrease computational time, the part was modelled symmetric over the XY and the XZ-plane. The fracture was expected to go along the x-axis, and a fine mesh was therefore used along that path, as seen in Figure 4.16. The size of the smallest elements modelled was 0.05 mm in all directions for simplicity.

During the analysis, the energy balance for the numerical model was checked. The amount of kinetic energy was found sufficiently low for a quasi-static behaviour, while the increase of the velocity kept the computational time low. The amount of artificial energy was also low, and the measured total energy was constant during the analysis indicating a stable analysis. This was considered satisfactory to go on with the model.
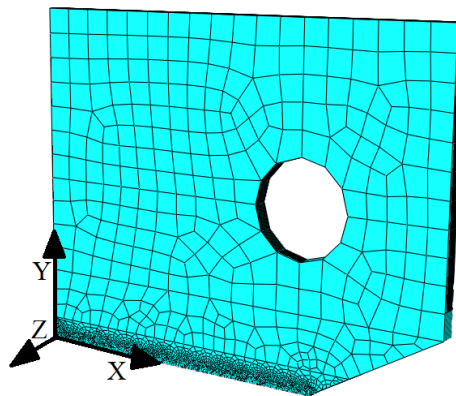
Figure 4.16: Illustration of mesh and coordinates of numerical Kahn model.

Results numerical model

The numerical model was validated using a force-vector elongation curve compared to the results from the experimental data. The force was taken from the XZ-symmetry plane. The vector elongation was found by specifying a vector corresponding to the vector used in the DIC analysis. This was done by measuring the deformation at a given point in the

model and dividing it by the initial distance between the point and the symmetry plane. The distance was half of the length of the DIC vector to account for symmetry. As the vector elongation was found to be dependent on the vector length, a shorter vector was also defined corresponding to a shorter vector in the DIC analysis. The relation between the results was the same, proving that the vector elongation from the DIC results and the numerical model corresponded as long as the vector length was the same. The points chosen for the two vectors can be seen in Figure 4.17. For further studies, only the longest vector was chosen, and the force-vector elongation compared to Kahn test 2 is seen in Figure 4.18. What is observed is that the numerical results nearly follows the shape of the experimental results, but the force is too high. This will be investigated in the parameter-study in section 4.2.3.
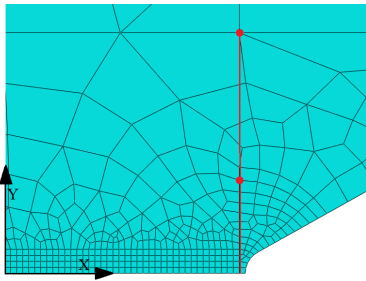

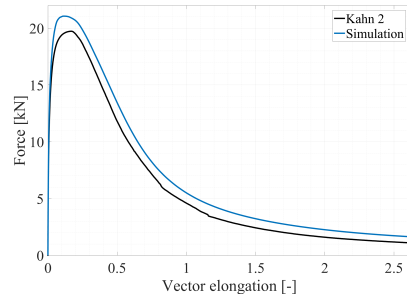**Figure 4.17:** Mesh in the notch, details from Figure 4.16.

Figure 4.18: Results from experiments and simulation of Kahn specimen.

4.2.2 Numerical model troubleshooting

In an attempt to find out why the forces in the numerical Kahn simulations were too high compared to experimental data, different changes to the numerical model were carried out. A first thought was that the use of boundary conditions and symmetry might have influenced the results, so this was investigated.

Further on, the pressure sensitivity of the material was considered by using the Drucker-Prager material model, as this decreased the stress levels a bit for the tensile tests in the material simulations. The reason why the stress levels were too high for the tensile specimens was the geometry of the notch. Therefore, this was also investigated as a possible reason for the not so good results in the simulation.

Another possibility was that the loading could be applied differently in the simulations. Instead of using a coupled constraint in the bolt holes, a rigid part was made to simulate the bolts, and the displacement was applied to the rigid part. The shape of the elements was also considered a source to the slightly wrong shape of the force - vector elongation curve.

The investigation of the numerical Kahn model did not cause the forces to decrease although the shape of the response curve was slightly improved. As the numerical model seemed to have no severe faults, further investigations of the test specimens were done, both on an undeformed and the deformed specimens. It was found that plastic deformation had taken place around the bolt holes after deformation on all specimens. These should

not be able to deform as all the plastic deformation should take place inside the notch. The reason for this was investigated, and new simulations were conducted.

Simulation

- The numerical model of the Kahn specimen had XY and XZ-symmetry. To be certain that this did not affect the results, new models were made. Figure 4.19 shows the results when removing the symmetry in the XY-plane. The only consequence was a little change in the shape of the curve. When modelling the part without XZ-symmetry, or with no symmetry at all, the results were identical to the simulation without XY-symmetry. It was concluded that this was not a problem with the numerical model.
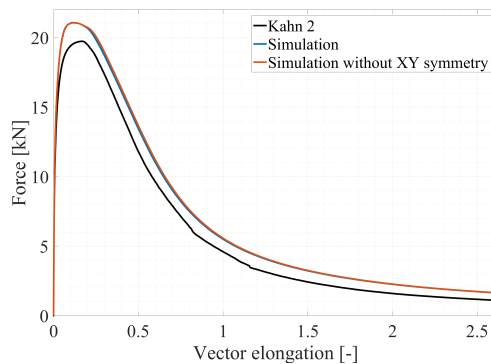

Figure 4.19: Effect of no XY-symmetry on Kahn simulation, compared to experimental data.

- When applying the Drucker-Prager criterion with β=2.3, K=1 and ψ=0 the effects were the same as for the tensile tests. The force level was only decreased by approximately 1%.

- In the simulations of the tensile tests, the problem was clearly the notch geometry. Therefore, this was investigated for the numerical model of the Kahn specimen too. The bottom of the notch was therefore flattened out so that the radius in the bottom of the notch was larger than 0.2 mm. This did not contribute to decrease the force magnitude for the simulation of the Kahn specimen, and so the geometry of the notch was not further examined.

- In the numerical model, the load was applied to the centre of the coupled constraint in the upper bolt hole. In an attempt to make the simulations more similar to the experiments, the coupled constraint was replaced with rigid bolts. A velocity was applied to the bolt going through the upper bolt hole. The bolts were made as analytical rigid parts with a radius of 3.99 mm. Surface-to-surface contact with a frictionless behaviour was applied between the bolts and the bolt holes walls. The

bolts were free to rotate. The result is presented in Figure 4.20, where the displacement is shorter than for the original simulation to reduce computational time. The shape of the curve was affected, but the difference is minimal.
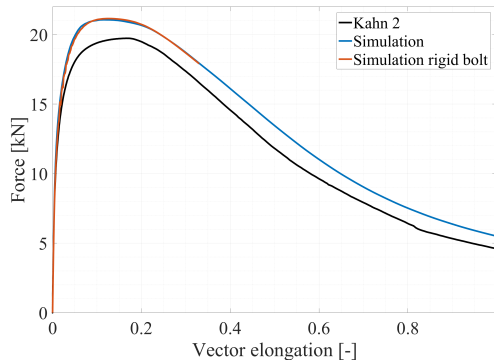
Figure 4.20: Effect of applying the load to the upper rigid bolt in the simulation, compared to using coupled constraint and experimental data.

- The mesh in the numerical model was made quadratic, like Sævareid did in his thesis (Sævareid, 2017). The same element shape as used in the numerical model of the Smooth tensile test was applied to the Kahn numerical model, so that $l_x = l_z = 0.0054$ mm and $l_y = 0.035$ mm. The result is shown in Figure 4.21, with a shorter elongation than the original to reduce computational time. The different element shape affects the shape of the curve a little, making it more similar to the experimental data. The curve is shifted more to the right, and the vector elongation at maximum force is more aligned.

Figure 4.21: Effect of changing the element shape on Kahn simulation, compared to experiments.

Specimen geometry

In the previous study, no obvious faults in the material model were found. It was there-fore decided to examine the experimental specimens once more, and the deformed and undeformed specimens were both inspected carefully.

- An undeformed test specimen was examined first. Using a micrometre, the thickness variation in the specimen was measured. The different values are shown 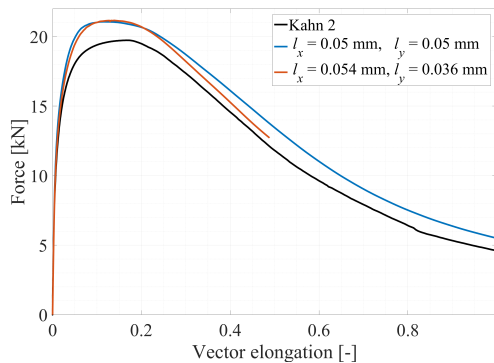in Figure 4.22. It is clear that the thickness is not uniformly equal to 2.54 mm, as the machine drawing in Figure 4.2 states. The effect of the varying thickness was investigated by running two simulations with thickness 2.52 and 2.56 mm. The results are seen in Figure 4.23.
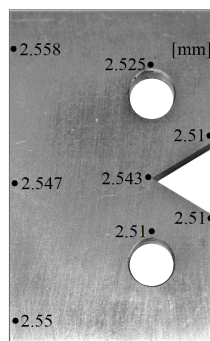
Figure 4.22: Measured thickness of the undeformed Kahn specimen using a micrometer.
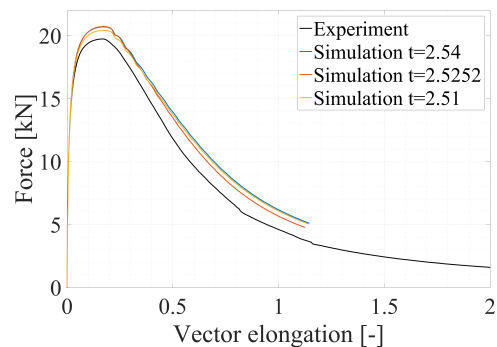
Figure 4.23: Force - vector elongation for the Kahn simulation with thickness 2.54, 2.525 and 2.51 mm, compared to experimental data.

- When investigating the deformed specimens, it was observed that the bolt holes were deformed into a slightly oval shape. Also, some of the parts were deformed plastically in Z-direction around the holes and at the crack path. The far ends from the notch were especially deformed in the tests with the largest displacement. Some thickness values were measured and written down for comparisons with the numerical model, and these are seen in Table 4.1.

  The holes were concluded to be deformed because of the size of the bolts, which must have had a different size than the holes during the experiments. This was controlled, and the bolts were confirmed to have a 0.1 mm smaller diameter than the holes. The diameter of the bolts was found to be 8 mm, while the diameter of the undeformed bolt holes was 8.1 mm.

4.2.3 Improved numerical model

The previous findings meant that both the geometry and the mesh of the original numerical model had to be changed. As seen in Figure 4.16, the mesh at the far end from the notch was fine in the original numerical model, and from the previous simulations, it was found that the representation of the deformation in Z-direction was satisfactory. To be able to

represent the plastic deformation in Z-direction around the bolt holes, the mesh close to the bolt holes was made considerably finer.

When changing the shape of the elements, from $l_x = l_y = l_z = 0.05$ mm in the original numerical model to $l_x = l_z = 0.0054$ mm and $l_y = 0.036$ mm, the shape of the response curve seemed to improve when comparing it to the experimental data, as shown in Figure 4.21. Hence, the shape of the elements was changed so that $l_x = l_z = 0.0054$ mm and $l_y = 0.036$ mm.

A previous analysis also revealed that when modelling a rigid part instead of using a coupled constraint in the bolt holes, the shape of the force - vector elongation curve was slightly improved, as Figure 4.20 shows. Therefore, this was investigated after changing the original numerical model as described above. The bolts were given the same diameter as in the experiments, 8 mm, while the bolt holes were expanded to 8.1 mm. Figure 4.24 shows the force - vector elongation curve for the different scenarios, and it is clear that when modelling the rigid bolts, the shape of the curve matches the experimental data better.
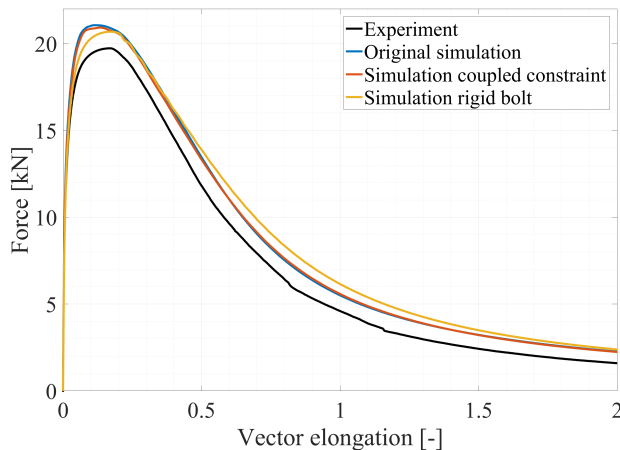
Figure 4.24: Effect of modelling the bolts as rigid parts, versus using a coupled constraint in the bolt holes, compared to experimental data.

The updated mesh and geometry of the improved numerical model are shown in Figure 4.25 and 4.26, respectively. Figure 4.25 also shows the modelled rigid bolt through the bolt hole. General contact with surface pairs was applied between the bolts and the inner side of the bolt holes, as it gave the same results as applying surface-to-surface contact. The upper bolt was moved in Y-direction with a velocity of 1000 mm/s, while the lower bolt was fixed. Both the bolts were free to rotate. To reduce computational time, the improved numerical model was modelled with XY and XZ-symmetry.
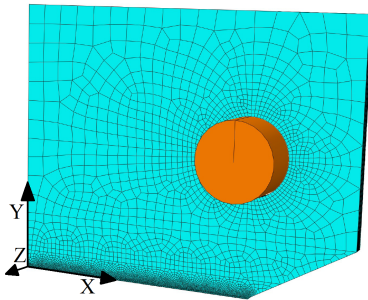
Figure 4.25: Mesh of the improved numerical model.
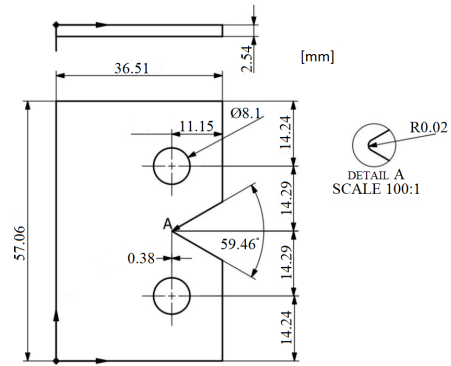
Figure 4.26: Geometry of the improved numerical model.

The force - vector elongation curve for the improved numerical model, the experimental data and the original numerical model is presented in Figure 4.27. The curve for the improved numerical model oscillates after maximum force. This could be improved by decreasing the velocity of the applied load, but in order to keep the computational time acceptably low the results are found satisfactory. The shape of the curve for the improved numerical model followed the experimental data better than the original numerical model before maximum force, but the estimated force was still too high. In the following section, a parameter study on the improved numerical model will be carried out. Here, the velocity of the simulations is 1500 mm/s to reduce computational time. It was controlled that when decreasing the velocity from 1500 mm/s to 1000 mm/s for the improved numerical model, the response curve was unchanged. The only effect of the velocity increase was a tiny increase in oscillations after maximum force, which was found acceptable.
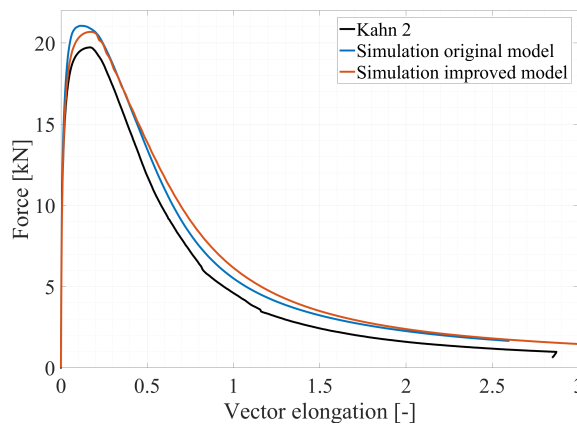
Figure 4.27: Response of the improved numerical Kahn model compared to experimental data and the original numerical Kahn model.

Parameter study

As presented in section 4.2.2, the thickness of the Kahn specimen is not uniform, as shown in Figure 4.22. The largest difference found from measurements were 0.048 mm. The thickness along the crack path only differs with 0.007 mm from 2.54 mm, which is acceptable. However, as the bolt holes deform plastically, the thickness there might have been of importance. The thickness of the bolt holes was measured to be 2.51 mm. For that reason, a study on the effect of changing the thickness of the improved numerical model was carried out. Figure 4.28 shows the response when changing the thickness to 2.525 and 2.51 mm, compared to the improved numerical model with thickness 2.54 mm. When the thickness was decreased, the resulting force was decreased, while the shape of the curves was similar. The reduction in force was expected since the area in which the force was applied to was decreased.

The effect of mesh size around the bolt holes was also investigated, to make sure that the plastic deformation of the holes was represented properly. In the improved numerical model, the mesh size at the holes was 0.3 mm. The mesh size was decreased to 0.1 mm around the holes, and the results are presented in Figure 4.29. The mesh modification leads to a modest decrease of the force level.
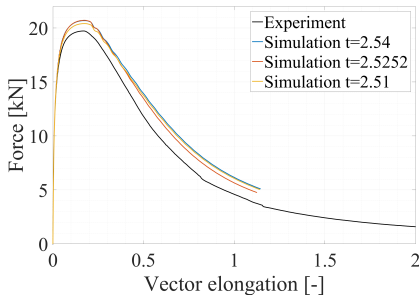
Figure 4.28: Effect of changing the thickness from 2.54 mm to 2.525 mm and 2.51 mm for Kahn in the numerical model, compared to experiments.
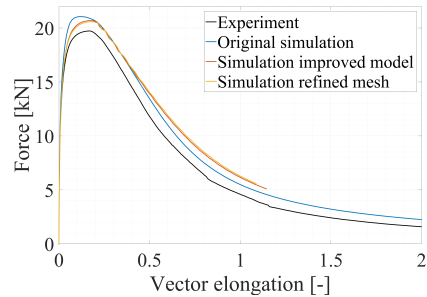
Figure 4.29: Effect of finer mesh at the bolt holes for Kahn in the improved numerical model, compared to the improved numerical model, the original numerical model and experiments.

To further investigate the relationship between the experiments and the simulation, the plastic deformation in the thickness direction was considered. The thickness of the deformed Kahn specimens was measured at the far end from the notch and at the bolt holes with a micrometre, position B and A in Figure 4.30, respectively. The thicknesses measured are presented in Table 4.1. It was found that the thickness at A was consistently larger for one of the holes, in all experimental tests. The values for A in Table 4.1 are therefore the thicknesses measured at the hole with the largest thickness.

Table 4.1 also presents the thickness at position A and B in the simulation of Kahn. The maximum elongation for the different Kahn tests was listed, and the thicknesses at point A and B were measured for the same elongations in the simulation. The thickness at the far end from the notch increases the longer the crack goes both in the simulation and the experiments. The thickness change at the bolt holes does not behave consistently in the experiments, while in the simulations it slightly decreases.
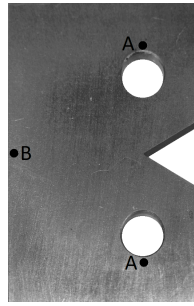
Figure 4.30: Positions A and B of measurements on Kahn specimens.

Table 4.1: Measured thickness in deformed Kahn specimens for both simulations and experiments. The tests are presented in ascending order, considering the displacement.

	Thickness A - bolt holes		Thickness B - end	
	Experiment [mm]	Simulation [mm]	Experiment [mm]	Simulation [mm]
Kahn 3	2.83700	3.28444	2.61400	2.60770
Kahn 4	2.86900	3.28399	2.74656	2.65420
Kahn 5	2.83500	3.28349	2.79700	2.93200
Kahn 2	2.88000	3.26671	3.15800	3.39320

4.2.4 Tunnelling in CT scans and improved numerical model

As mentioned in section 4.1.2, tunnelling is a phenomenon that often occurs in ductile fracture, and a good model to predict tunnelling is the GTN model as it uses accumulated damage along the crack front as a growth criterion. A problem with the GTN model is that it relies upon high levels of triaxialities to drive the damage process. This makes it less applicable for thinner specimens, where the void growth and coalescence process more typically occurs along bands of large plastic strain (Gullerud et al., 1999).

Many studies have been done on the phenomenon of tunnelling, and other approaches have also been proven to be effective in regards to this. A growth criterion that has been successful in predicting tunnelling is the Crack Tip Opening Angle (CTOA). This is an approach that controls the crack growth by advancing the crack front a prescribed distance when the CTOA reaches a specific critical value, and the crack will typically extend one element size at a time through node release procedure (Gullerud et al., 1999).

This method was extended to 3D by Gullerud et al. (Gullerud et al., 1999) by checking CTOA at each node along the crack front, and they were successful in predicting the tunnelling profile of an aluminium deep-notch single-edge specimen under mode I loading.

Zuo et al. (Zuo et al., 2004) have also done studies on this, focusing on the effect of the stress constraint on the CTOA value, and results proved that the Crack Tip Opening Displacement (CTOD) value decreased as the stress constraint increased.

Many studies have also been done on the effect of crack tunnelling on deformation

fields and structural response. Dawicke et al. (Dawicke et al., 1995) compared variations of the CTOA and a global constraint factor on straight and tunnelled cracks. This indicated that the effect the shape of the crack-front had on the global constraint factor was small, but had a stronger influence on the through-thickness CTOA. This was especially seen in the early stages of crack growth.

James & Newman (James and Newman, 2003) studied the effect of crack tunnelling on a predicted load-crack extension curve, and proposed a method based on the area average to calculate the effective crack extension. In this method, the average crack length was calculated using a formula to describe the measured surface crack length as well as the tunnelling magnitude. This produced a load-crack extension curve that corresponded well with the experimental measurements after the maximum load, but less with the early stages of crack growth.

Lan et al. (Lan et al., 2010) carried out three-dimensional elastic-plastic finite element analyses for tension-torsion specimens with straight and tunnelled cracks under remote mode I loading conditions. If was found that crack tunnelling raised the levels of CTOD, the effective stress and the effective plastic strain on the specimen surfaces, and also lowered the mean stress and the stress constraint levels on the specimen's mid-plane.

In this thesis, the main focus is to investigate the GTN model further, and in this section, the results from the CT scan and the numerical results using GTN will be studied more closely to investigate the tunnelling and the relation between crack length and tunnelling. The amount of tunnelling for different crack lengths will be studied.

CT scans and improved numerical model

The Figures 4.31 and 4.32 shows the CT scans of the experiments and the simulation for the Kahn tests 3 and 5, respectively. Figure 4.31b is taken from the simulation when the elongation coincides with the elongation of the specimen in Figure 4.31a. This also applies to the Figures 4.32b and 4.32a. The simulation was not set to write the field output for every unit of time, and therefore the elongations may not be exactly the same. The red line in the Figures 4.31a and 4.32a indicates, with a slight margin of error, where the tunnelling starts. Figures 4.31b and 4.32b are cut in the middle of the XY-plane to demonstrate the tunneling.

In both Figure 4.31 and 4.32 it is seen that the crack length is longer for the experimental results, while the tunnelling is longer for the numerical model. Figure 4.33 shows the relation between the crack length and the length of the tunnelling for the 4 Kahn tests and different values from the numerical model corresponding to different elongations. Also here it is observed that the tunnelling lengths are longer for the numerical model, while the crack lengths are longer for the experimental results. Common for both is that the length of the tunnelling increases in the beginning and then decreases after a certain point. This behaviour was also observed by James & Newman (James and Newman, 2003), observing that tunnelling would initially increase as the fracture region developed, and then decrease as the shear lips formed with increasing plasticity and stabilise at a constant value.

Another interesting observation is that the crack seems to develop faster at the end of the experiment. This could be due to less tunnelling making the crack propagate faster.

(a)   **(b)**
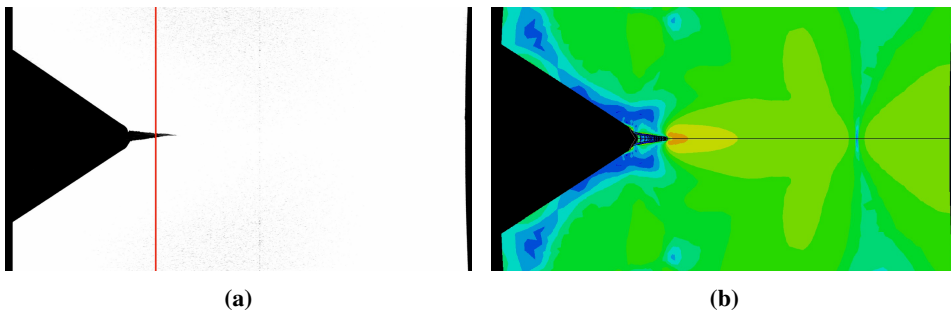
Figure 4.31: Comparisons of experimental and numerical model for Kahn specimen 3.

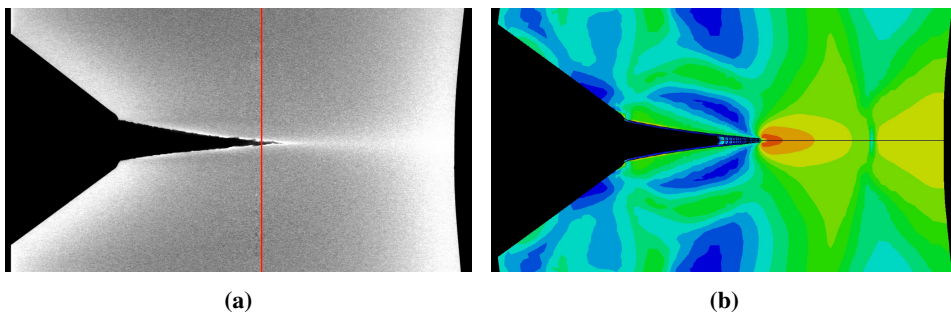**(a)**   **(b)**

Figure 4.32: Comparisons of experimental and numerical model for Kahn specimen 5.
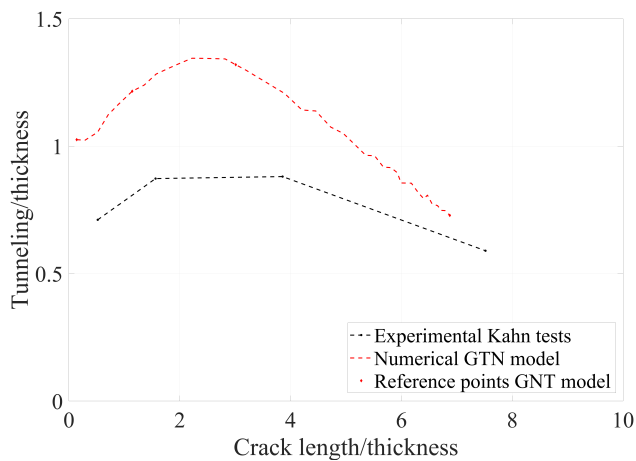

Figure 4.33: The relation between tunnelling length and crack length for the numerical model and the experimental results. The reference points of the GTN model represents the similar location in the analysis as the experimental results.

Figure 4.34 illustrates the tunnelling in the simulation. Figure 4.34a shows the onset of tunnelling, whereas Figures 4.34b and 4.34c shows the tunnelling at the elongations similar to the Kahn specimens 3 and 5, respectively.
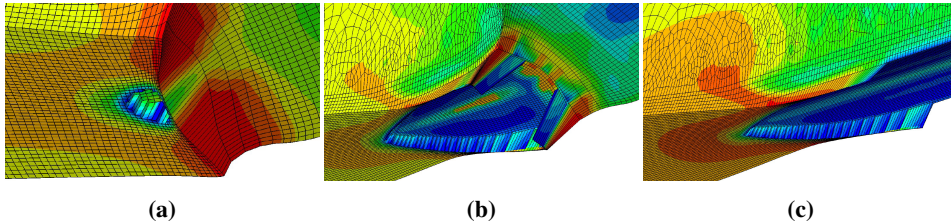

| (a) | (b) | (c) |

Figure 4.34: Illustration of tunnelling in the numerical model in **a)** the onset of tunnelling, and for elongations corresponding to Kahn specimens **b)** 3 and **c)** 5.

4.2.5   Evaluation of results

Based on the results from the previous section, the final numerical model was slightly changed from the original numerical model. It was found that during experiments, the bolts were 0.1 mm smaller than the diameter of the bolt holes. This resulted in plastification around the bolt holes, while only the crack path was plastically deformed in the original simulation. When accounting for this, the results were improved. Even though the shape of the force - vector elongation curve based on the simulation seemed to match the experiments perfectly, the maximum force was about 5% higher than the experimental data.

- The GTN model does not account for pressure sensitivity of the matrix material, which contribute to the overestimation of the forces due to high triaxialities in the sharp notch. When applying the Drucker-Prager criterion, the maximum force was slightly decreased.

- When investigating the undeformed Kahn specimen, it was found that the thickness was not uniform. By decreasing the thickness of the specimen, the stiffness was decreased too. The variation of the thickness, and other imperfections such as inhomogeneity in the material, may be a reason for the overestimation of the forces in the simulation.

- It was found that the diameter of the bolt holes was larger than what the machine drawing stated. For small specimens, there is a higher chance of errors due to machining, as experienced for the tensile tests R08 and V45 in chapter 3. As the geometry of the specimens was controlled only manually with a micrometre, small errors due to the geometry in the numerical model may have occurred. A critical dimension was the position of the centre of the bolt holes compared to the notch. If the centre of the bolt holes were to be more aligned with the notch, meaning being moved a 0.38 mm distance, the crack would initiate earlier due to the increased value of the moment, and the resulting forces would decrease.

- When accounting for the different diameter of the bolts and the bolt holes in the improved numerical model, the shape of the force - vector elongation curve was improved. The displacements in the thickness direction at the bolt holes for both experiments and simulation tend to stay constant after the point where plastic deformation localises in the notch. However, in the simulation, the maximum displacement was 3.28 mm, while it was 2.88 mm in the experiments. As the plastification around the bolt holes was too large in the simulations, it may indicate that the relation between the diameters of the bolts and the bolt holes were inaccurate. In the original numerical model, the plastification at the bolt holes was not accounted for, since the bolts had close to the same diameter as the bolt holes. The main (and most important in this case) difference between the two models was the shape of the curve before maximum force. Lowering the difference between the diameter of the bolts and the bolt holes would probably result in a curve laying somewhere in between the two simulations shown in Figure 4.27, which implies that if there were to be some tiny errors due to the relation, this would not contribute to lowering the forces.

- In the experiments, the crack starts to develop earlier than in the simulation. The comparison between the simulation and the CT scans shows that the simulation experiences more bending than the experiments at the same elongation, as the walls on the left-hand side in the Figures 4.31b and 4.32b indicates. In the experiments, the crack starts to develop in the neck before the rest of the specimen is deformed, while in the simulation the deformation outside the notch starts right before the onset of tunnelling. It appears that the problem regarding the stiffer curve from the simulation lies at the onset of the crack.

- The maximum thickness at the bolt holes in the simulation is 3.28 mm. At this point the simulation starts to fail from the middle, behind the notch, as Figure 4.34a shows. From here, further plastic deformation happens mainly in the notch, and the thickness of the bolt holes slightly decreases, as stated in Table 4.1. In the experiments, the change of thickness at the bolt holes is not consistent with elongation. This may be due to the friction between the bolts and the bolt holes. In the simulation, there is no friction applied between the bolts and the bolt holes, which is probably the reason for the consistent decrease in thickness after the onset of tunnelling.

- Due to friction in the experiments, restraint forces may occur as the bolts are not entirely free to rotate, which may be the reason for the earlier onset of cracking in the experiments, compared to the simulation.

- For both the experimental results and the numerical GTN model, the relation between the tunnelling and the crack length seems to increase in the beginning of the analysis, then to decrease after a certain point. A difference in the length of the tunnelling for the two is that the tunnelling is a bit longer for the numerical model, while the crack length is longer for the experimental results. This could be connected to the force of the numerical model being too high, and the failure criterion being reached too soon in the middle of the thickness. The GTN model seems to predict fracture too soon for high triaxialities, and too late for low triaxialities in the elements, which leads to increased tunnelling and the fracture propagating too slow.

Chapter 5

Pipe simulation

5.1 Introduction

In this chapter, the application of CZ in crack-propagation studies for offshore steel will be investigated more closely. Material properties for the cohesive elements to be used in the pipe simulations will be calibrated from tensile tests simulated with the same thickness in Abaqus. These properties will be adjusted for and applied to a numerical model of the Kahn-test for validation. A numerical model for the pipe will then be established, and a parameter study will be carried out on the numerical model. A numerical model of the pipe using solely the GTN damage model will also be established.

If a running fracture were to happen in a pipeline, there are three different main events. The elastic-plastic deformation of the walls, the gas dynamics, and the inelastic behaviour of the propagating crack. The FE model of the pipe is relatively simple to create, so the true challenge is describing the dynamics of the gas and the propagation of the crack in a good way. In a pipeline, the initiation of the crack is triggered when a critical crack length is reached. When fracture has occurred, the gas flows rapidly out of the opening. This flow reduces the pressure around the opening and generates a decompression wave that propagates away from the opening, inside the pipeline. The speed of the propagating front depends on initial pressure, temperature, and the mixture of the gas that is inside the pipeline. The driving force of the crack depends on the global pressure decay in front of the crack tip, and the distribution of the local pressure at the flaps behind the crack tip. If this driving force exceeds the material resistance, the structure is unstable, and the crack will continue to propagate (Cleaver and Cumber, 2000).
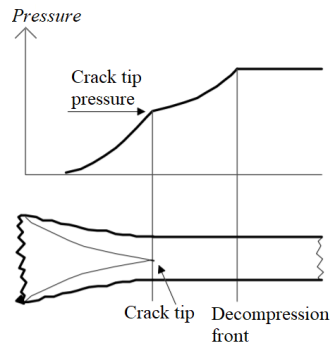
Figure 5.1: Illustration of crack tip pressure and decompression front of at a section of a pipe during fracture propagation. Figure taken from (Cleaver and Cumber, 2000).

There are several ways that may work when modelling the crack propagation. A mathematical model was derived and validated by Cleaver and Cumber (Cleaver and Cumber, 2000), based on known theory from shock tubes and real gas behaviour. They proposed to use the model to find out whether a crack would propagate or not. A more accurate method is to couple CFD and FE models, which is what was done by Nordhagen et al. (Nordhagen et al., 2012). When comparing with full-scale experiments, it is clear that Nordhagen et al. was successful in describing both the pressure evolution in front of the running ductile fracture and the crack position.

Scheider et al. (Scheider et al., 2014) modelled the crack propagation using only an FE model, by applying pressure to two different loading zones, one in front and one behind of the crack tip. The pressure profile behind the crack was described by an exponential function derived from full-scale experiments. The function was dependent on the pressure at the crack tip, the pipe circumference and the location of the crack tip. The pressure in the front of the crack tip was kept at the same value as the pressure at the crack tip. The initial pressure was set to 72% of the yield strength, and then the crack tip pressure was linearly reduced to 40% of initial pressure in 20ms.

In this study, a uniform pressure will be applied, without considering the location of the crack tip. The initial pressure will be linearly decreased as done by Scheider et al. and applied to the pipe's inner surface using one loading zone. Schneider et al. presented the fracture resistance curves used, which represented the relation between the crack velocity and the pressure level.

The main focus of this final chapter is to develop a cohesive zone model of the pipe and find the parameters influencing the wall deformation and the length of the propagated crack when changing the element sizes, loads and boundary conditions in the simulations.

5.2   Cohesize zone in Abaqus

In fracture mechanics, the use of cohesive zone has been an important evolution in the field and is widely used to simulate crack initiation and propagation in solids when the crack path is known. A major advantage in the use of the CZ model is that it describes the crack propagation in a robust and efficient manner over long distances (Nonn and Kalwa, 2013). The cohesive zone does not represent any physical material but rather describes the cohesive forces that occur when the material elements are being pulled apart (Salve and Jalwadi, 2015). The cohesive interface elements are defined between the continuum elements and will open when damage occurs and lose their stiffness at failure, resulting in continuum elements disconnecting (Scheider, 2018). This way of modelling is different from using the GNT model as no continuum elements are damaged in the CZ model.
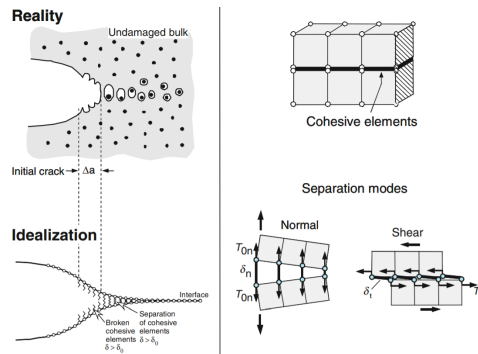
Figure 5.2: Cohesive zone as illustrated by Schwalbe et al. (Schwalbe et al., 2013).

In Abaqus, a way to create a cohesive zone model is to use cohesive elements. Cohesive elements are fully nonlinear elements that can be used with finite strains and rotations and can also be given a mass in dynamic analyses (Abaqus, 2016). An illustration of cohesive elements can be seen in Figure 5.2. The connectivity of these cohesive elements is like the continuum elements, but it is useful to think of cohesive elements as two faces separated by a thickness (Abaqus, 2016). The cohesive zone must therefore be discretised with a single layer of cohesive elements through a small zero-like thickness.

When the cohesive element layer is sufficiently thin, the cohesive behaviour can be defined in terms of a traction-separation law. This is useful in fracture mechanics when modelling delamination at interfaces and is defined in Abaqus by choosing a traction-separation response when defining the section behaviour of the cohesive elements. A damage initiation criterion is also specified, and the initial response of the cohesive element is assumed to be linear until the damage initiation criterion is met. A way to specify the damage criterion is to specify the maximum nominal stress criterion, which assumes damage initiation when the maximum nominal stress ratio reaches a value of one, defined as MAXS in Abaqus.

Figure 5.3: Illustration of traction-separation curve for the matrial, inspired by Abaqus Analysis User's Manual (Abaqus, 2016).

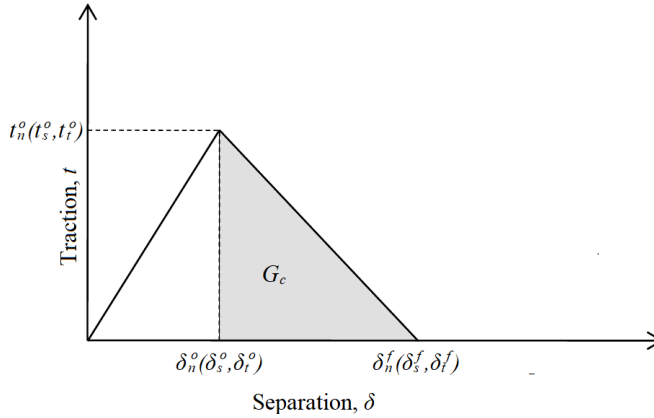Figure 5.3 illustrates the traction-separation curve used in MAXS damage in Abaqus, where t is the traction stress vector, consisting of three components t_n, t_s and t_t which represents the normal and two shear tractions in a 3D element. The separations corresponding are denoted by δ_n, δ_s and δ_t. t_n^o represents the peak values of the nominal stress. When using the damage criterion MAXS damage in Abaqus, damage initiates when the maximum nominal stress ratio, defined in equation 5.1 reaches the a value of one (Abaqus, 2016). For cases of pure compressive deformation or stress damage will not initiate.

$$max\left(\frac{t_n}{t_n^o}, \frac{t_s}{t_s^o}, \frac{t_t}{t_t^o}\right) = 1 \tag{5.1}$$

The damage evolution can also be specified, describing the rate at which the material stiffness is degraded once the corresponding initiation criterion is reached. A scalar damage variable D represents the overall damage in the material and captures the combined effects of all the active failure mechanisms. It initially has a value of 0, and as the loading continues after initiation of damage it evolves to 1.

Damage evolution can be defined based on fracture energy, G_c, which is the energy dissipated as a result of the damage process. The fracture energy is equal to the area under the traction-separation for the curve, as can be seen in Figure 5.3 and is specified as a material property. When the fracture energy is defined, Abaqus ensures that the area under the damage response is equal to the fracture energy. In Abaqus, this fracture energy is defined as energy per area to be separated, given as [N/unit].

In this thesis work fracture energy is used as a damage evolution criterion. The idea is that cohesive elements can be used instead of GTN to simulate the crack propagation, as this will make the modelling easier and the CPU time smaller as the mesh size required for CZ can be larger. The fracture energy is then found from simulations using the GTN model, and the procedure is explained further in the following sections.

5.2.1 Tensile test to calibrate fracture energy

To find the fracture energy for a plate with a specific thickness, Hutchinson & Nielsen (Hutchinson and Nielsen, 2012) performed an analysis on a plane strain finite element model of a tensile test with width like the specified thickness and a constant thickness. The GTN model was used as material input, and the force-displacement from the analysis was used to find a traction-separation curve and the dissipated energy from the analysis. The dissipated energy was found as the area under the traction-separation curve, and both the dissipated energy due to necking and the dissipated energy due to shear localisation and fracture was identified. The dissipation generated during necking prior to the onset of shear localisation was found to be the dominant contribution, and this was found sufficient to describe fracture energy for most cases. Hutchinson and Nielsen also introduced a very small asymmetric imperfection in the yield stress distribution to provoke this kind of fracture, as well as other studies on how to establish the fracture energy.
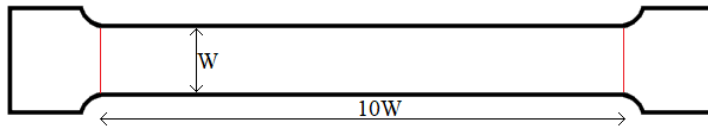

Figure 5.4: Dimensions and geometry of plane strain tensile test for calibration of fracture energy.

A conclusion for Hutchinson and Nielsen was that the dissipated energy from necking was sufficient to calculate the fracture energy. As this method proved to be successful for Hutchinson and Nielsen, the same procedure was done in this study to calibrate the CZ parameters fracture energy and nominal stress. The parameters were found for two cases, a 2.54 mm thick Kahn tearing test and a 6 mm thick pipe wall. A tensile test as seen in Figure 5.4, with material properties and mesh size found in Table 3.4 was run until fracture. The thickness was 1 mm for both cases, and the width the same as the specimen thickness. From the force-displacement curve, a traction-separation curve was established. The point of necking was found as the point of maximum load, and the point of shear localisation was found as the point of critical failure. Figure 5.7 and Figure 5.9 shows the traction-separation curve for the Kahn test calibration and the Pipe calibration respectively. The traction, t, is described by Equation 5.2, while the separation, δ, is described by Equation 5.3.

$$t = \frac{F}{\sigma_Y * A_0} \tag{5.2}$$

$$\delta = \frac{\Delta - \Delta_0}{W} \tag{5.3}$$

Where Δ and Δ_0 represents the displacement and displacement at maximum force, and W is the width. The area under the graphs represents the fracture energy for the different widths and describes the energy it would take for the two continuum parts to separate in a cohesive zone model. For the input in Abaqus, the fracture energy found was divided by

the area at which the force was working to find fracture energy per area. As the thickness was 1 mm, the area, A_0 had the same value as the defined width. The fracture energy input in Abaqus was found by Equation 5.4

$$G_c = \frac{\int_0^{\Delta_{max}} F d\Delta}{A_0} \tag{5.4}$$

The nominal stress was also found as the force components divided by the original area as:

$$\sigma_N = \frac{F_{max}}{A_0} \tag{5.5}$$

The cohesive zones in the following numerical models will be assigned the CZ model material described by the nominal stresses for the maximum stress damage and the fracture energy for the damage evolution. The remaining parts of the model will be given the material Steel, which is described by the elasticity constants, the density, and the work hardening by Power law described in Table 3.4. As the crack path is known, the CZ will represent all the failure in the elements, substituting the failure properties of the GTN model.

5.3 Validation by Kahn

To validate the use and calibration of the CZ model, a numerical model of the Kahn specimen was made with the geometry given in Figure 4.26. The model was given a velocity of 1000 mm/s. The bolts were modelled as kinematic couplings in the bolt holes. Instead of a coarse mesh close to the crack patch, a 0.001 mm thick section with 8-node three-dimensional cohesive elements, COH3D8, was created at the XZ-symmetry plane, as Figure 5.5 shows. The elements were given a stack direction normal to the elements, i.e. in Y-direction. The tiny band was assigned a cohesive section with a traction separation response, and the CZ model material. The rest of the part was assigned the elements C3D8R and the material Steel which is described at the end of section 5.2.1. The fracture energy and the nominal stress for the CZ material were found from a tensile test as described in section 5.2.1, with a thickness the same as the Kahn test, 2.54 mm. The traction-separation curve is presented in Figure 5.7, and the nominal stress and fracture energy were found to be 757.9 MPa and 969.1 N/mm, respectively. Figure 5.6 shows how the cohesive elements deform and then erode when the CZ damage criterion is reached. The computational time when using CZ elements instead of the GTN model was dramatically decreased.
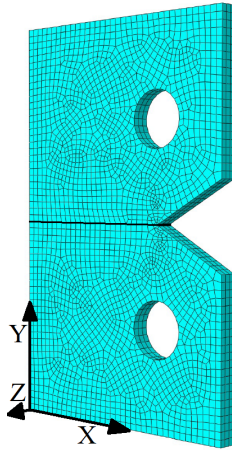
Figure 5.5: Mesh of the Kahn numerical model with element size of 1 mm and the cohesive zone illustrated as the black line.
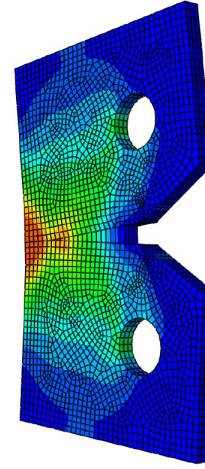
Figure 5.6: Illustration of the deformed numerical model of Kahn with CZ elements.

A mesh study was carried out to see if the size of the elements influenced the response curve. The numerical model was given three different element sizes of 0.5 mm, 1 mm and 1.7 mm. This was also the size in X and Z-direction for the cohesive elements. The force-elongation curves for the numerical model with the three different meshes are presented in Figure 5.8, together with the experimental data and the response from the GTN numerical model. From the figure, it can be seen that the results of the CZ model are close to identical even though the mesh size has changed.
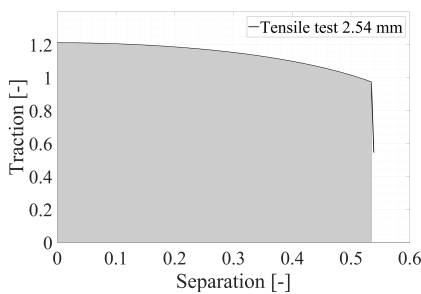
Figure 5.7: Traction versus separation curve for the 2.54 mm tension test.
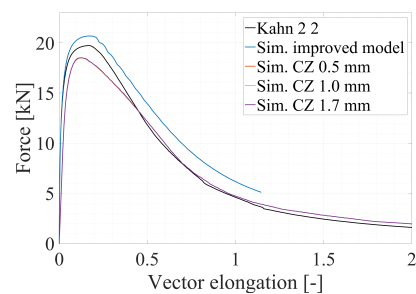
Figure 5.8: Effect of changing the element size on the cohesive elements, compared to experimental data and the GTN improved numerical model.

The cohesive zone is a substitution for the failure properties of the GTN model, so all the failure should occur in the CZ, meaning the model is not able to capture void nucleation

and coalescence, but only the elastic and plastic response. As seen in Figure 5.8, the CZ model is not able to capture the softening at large strains perfectly. This was expected as the softening behaviour is due to the void growth which the GTN numerical model is able to describe. Aside from this, the CZ model represented the curve well, despite a 17 % underestimation of the forces compared to the experimental results. The reason for the conservative results could be due to less local deformation of the specimen outside the cohesive zone compared to the GTN numerical model.

The overall conclusion is that the CZ model manages to capture the force-elongation for the Kahn-test in a satisfying manner, and the method for calibrating the CZ parameters will be used in the same manner for the pipe.

5.4 Pipe simulations

As described in section 5.1 there are several ways to describe a running fracture in a pipe, where some are more accurate than others. The biggest challenge when simulating gas flowing through a pipe is how to model the load that appears due to depressurisation once the crack is initiated and starts to propagate. A coupling between CDF and FE models is the simulation that will be the closest to reality. However, when trying to simplify the simulation by using only an FE model, other methods are required. Schneider et al. modelled the pressure by using two different loading zones, one behind and one in front of the crack tip (Scheider et al., 2014). The pressure behind the crack tip was described by a function depending on the position of the crack tip, while the pressure in front of the crack tip was equal to the pressure at the crack tip. In the following, a simplified numerical model of a pipe with a running crack will be presented.
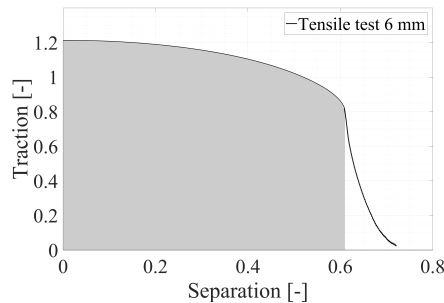
Figure 5.9: Traction versus separation curve for the 6 mm tension test.

5.4.1 Calibration of the cohesive material parameters

The calibration of the CZ parameters for the numerical model of the Pipe was done as described in Section 5.2.1. The pipe modelled had a wall thickness of 6 mm, and the calibration was done with a width of 6 mm to represent this. Figure 5.9 shows the resulting traction-separation curve for the tensile test. In the figure, the damage initiation is represented by zero separation, and the critical damage by a separation of 0.6. The resulting

nominal stress and fracture energy were 757.9 MPa and 2552.9 N/mm respectively.

5.4.2 Numerical model

Two different approaches for modelling the cohesive zone were tested, one where the cohesive zone was modelled as a different part and connected to the rest of the pipe using tie constraint, and one where the pipe was modelled as one part and partitioned to define the cohesive section. The model using tie constraint will from here on be called model A, and the model using partitioning will be called model B. The two different approaches curiously gave quite different results, something that will be discussed in the parameter study in section 5.5. Besides this, the models were identical and modelled as described below.

The pipeline dimensions were D_o = 267 mm and t = 6 mm, the same as the test pipes used by Nordhagen et al. The length of the numerical model was set to 6000 mm, which is half of the test pipe they used (Nordhagen et al., 2012). A cohesive zone of 0.001 mm was modelled through the thickness and along the pipe, as the red and black lines indicates in Figure 5.10. The cohesive zone was modelled with an 8-node three-dimensional cohesive element, COH3D8. The black line in Figure 5.10 was assigned with the cohesive parameters calibrated from the 6 mm tensile test. The cohesive zone marked with red in Figure 5.10 had a length of one diameter and was meant to initiate fracture. This was given a material similar to the CZ model, where the difference was that the fracture energy and the nominal stress constants were 10 % of the calibrated ones presented in section 5.4.1. The rest of the model was modelled with C3D8R elements of size 20x20 mm, given the Steel material which is described in the end of section 5.2.1.
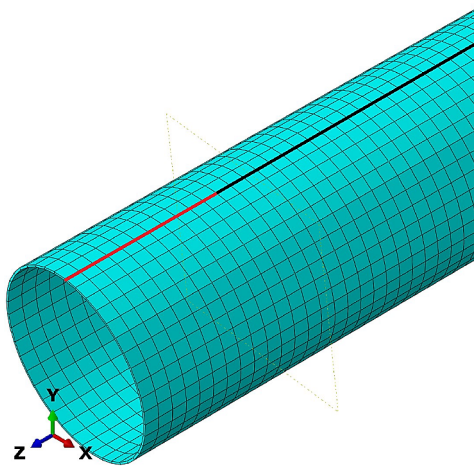

Figure 5.10: End of the modelled pipe with mesh. The red and black line illustrate the CZ.

Loading

Figure 5.11 illustrates the stresses that will occur in a thin-walled vessel or pipe when applying an internal pressure p, which are the hoop stress σ_θ and the longitudinal stress σ_L. The hoop stress is calculated by equation 5.6, where d is the mean diameter, p the pressure, and t the thickness (Irgens, 1996). The longitudinal stress in the vessel equals half of the hoop stress. When using equation 5.6, and a yield stress of 652.5, the pressure p becomes 29.65 MPa.

$$\sigma_\theta = \frac{d}{2t}p \qquad (5.6)$$
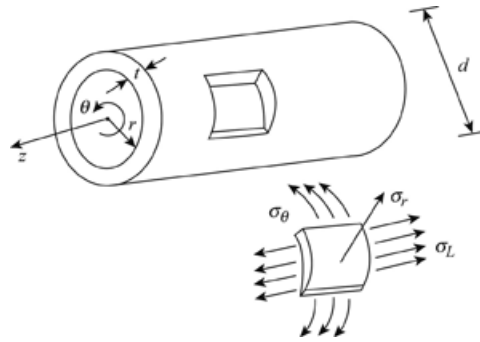
Figure 5.11: Illustration of the hoop stress and longitudinal stress in a pipe, figure from (Chegg, 2018).

Inspired by Schneider et al., an initial pressure p_0 applied in the FE model was 21.35 MPa, 72% of p (Scheider et al., 2014). The pressure was applied uniformly throughout the pipe. As a result of the cohesive zone marked in red in Figure 5.10, the crack initiated momentaneously when the pressure was applied, and the crack started to propagate. If the pressure was kept constant, the pipe started to expand. In the simulations by Schneider et al., the pressure at the crack tip was decreased to 40% of the initial pressure in 20 ms. Even though the pressure in the numerical model in this study did not depend on the crack tip, a pressure decrease was still essential. A study was done to find a suitable amplitude for the pressure decrease in the numerical model. The pressure was decreased to 40% of p_0, where the time period of the decrease was varied. After the decrease, the pressure was kept constant at 40% of p_0. A time period of 1 μs was found to be a good solution. When applying this pressure, the pipe did not expand too much, while at the same time the crack still propagated.

Mesh size

Before carrying out the parameter study in section 5.5, it was desired to find out the importance of the element size in the cohesive elements compared to the rest of the model. As mentioned in section 5.2, cohesive elements should be close to zero thickness, and only have one element across the thickness. As having the cohesive elements the same

size as the rest of the model would save modelling time as well as CPU time, a study was run with two different cohesive element sizes. 6 meters of the pipe was modelled with an initial crack with the length equal to the diameter 267 mm, and a global element size of 20 mm. In the first model the cohesive elements had element size 0.5 mm and in the second model the cohesive element size was the same as the global element size, 20 mm, both were modelled with three elements over the thickness to represent bending.
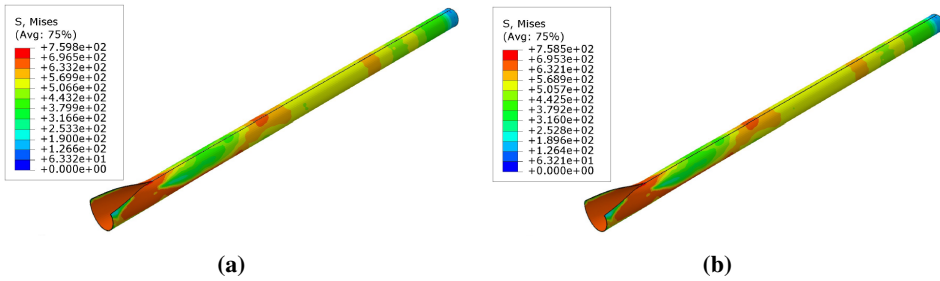
Figure 5.12: The deformed pipe using **a)** small elements in the cohesive zone **b)** big elements in the cohesive zone.

The deformed models with the two different element sizes in the cohesive zone are seen in Figure 5.12. Some results are shown in Table 5.1. The crack length measured is very similar for the two models, and the difference is less than one 20 mm element, meaning the difference in element size could be the reason. The dissipated energy is almost exactly the same, with a 0.2 percent difference in measured dissipated plastic energy. Perhaps the most noteworthy are the two different CPU times. The model with bigger elements uses almost 8 times more CPU time than the model with the smaller elements in the cohesive model.

Table 5.1: Crack length, disiipated energy and CPU time element sizes 0.5 and 20 mm in the cohesive zone.

Element size [mm]	Crack-length [mm]	Dissipated energy [J]	CPU time
0.5	424.0	4.78e9	726.2
20	419.9	4.77e9	91.0

These results indicate that it is reasonable to use cohesive elements with the same size as the global elements instead of smaller elements. The results from two analyses correspond well in crack-length, and the difference in dissipated energy is close to zero. Based on Abaqus user manual, the damage initiation and failure material properties defined for the cohesive elements seem to be independent of the mesh size, as both the fracture energy and nominal stress are found as the fracture energy divided by the total area to be separated. The most important is to have only one element over the thickness, something both models have.

5.5 Parameterstudy using the CZ model

Two parameter studies, varying the initial pressure and the mesh size, were carried out for the two cohesive zone models, model A and model B. As these two models gave different results, the value of the parameters were not completely the same for the two. For the mesh size, the previous section stated that it was reasonable to use cohesive elements with the same size as the global elements. No advanced meshing techniques were required to mesh the FE model, but the element size was found to be crucial. The element sizes studied in model A were 5, 10, 15, 20 and 30 mm, while in model B the element sizes were 5, 10, 17, 20 and 30 mm. The initial pressure was varied from 0.6 times the original initial pressure to 2 times the initial pressure for model A. A larger diameter expansion was observed for model B, and the initial pressure was varied from 0.6 to 1.1 times the original initial pressure. The results are presented below.

Parameter study model A
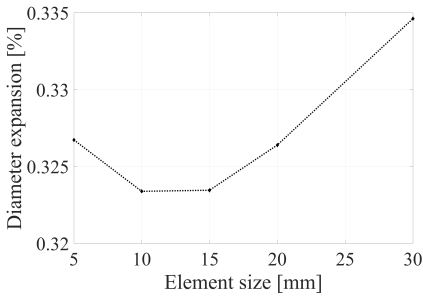
Figure 5.13: Expansion of pipe diameter versus element size model A.

Figure 5.14: Crack length versus element size model A.

Figure 5.15: Expansion of diameter versus initial pressure model A.
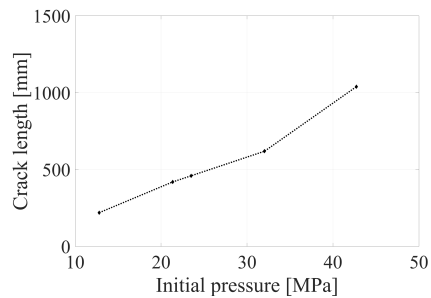
Figure 5.16: Crack length versus initial pressure model A.

Figure 5.13 shows the diameter expansion in measured difference in diameter divided by initial diameter for the mesh sizes 5, 10, 15, 20 and 30 mm. As the figure shows, the diameter expansion is low for all the element sizes run in the model, all of them showing an expansion less than 0.5 % of the original diameter.

The measured crack length for the different element sizes at the end of the analysis is seen in Figure 5.14. The crack length is measured as the length of the crack minus the initial crack length of one diameter. An increasing of the crack length is observed when the element size is increased. As the smaller elements would deform more and lose more energy to plastic dissipation, this is to be expected. Especially the model with element size 30 mm have deformed very little, and all of the energy is focused on propagating the crack. When looking at the plastic dissipation energy measured for the different mesh sizes, the plastic dissipation is highest for the smallest mesh size, and smallest for the biggest mesh size. This could indicate that the crack has propagated a shorter distance for the smaller mesh size because it has lost more energy through plastic dissipation.

Figure 5.15 shows the diameter expansion for different initial pressures. The initial pressures were 0.6, 1, 1.1, 1.5 and 2 times the original initial pressure found in section 5.4.2. It is apparent that the model could handle an increase of pressure for up to 1.5 times the original pressure found without the diameter expansion becoming too high. However, for a pressure 2 times the original, the diameter expansion increases rapidly, almost up to 40 %.

The crack length versus initial pressure is seen in Figure 5.16. The increase of the crack length compared to initial pressure seems to be almost constant, where the initial pressure leads to a crack length of around 1 meter.

Parameter study model B

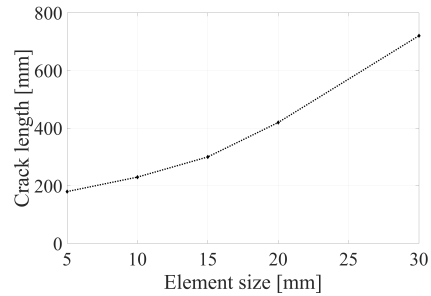**Figure 5.17:** Pipe diameter versus element size model B.

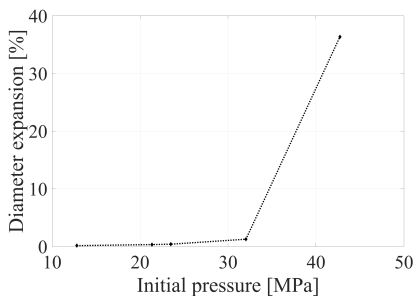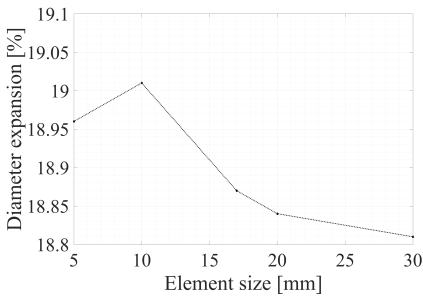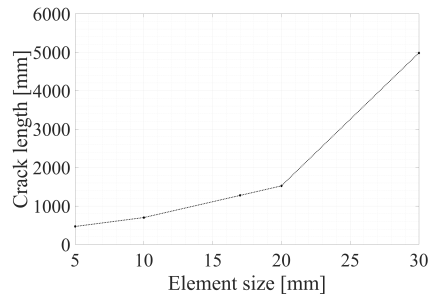
Figure 5.18: Crack length versus element size model B.
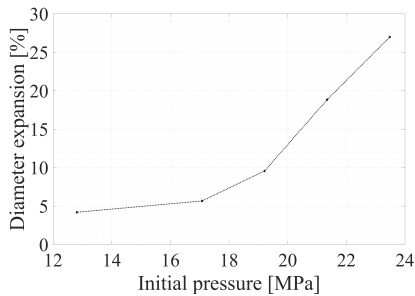

Figure 5.19: Pipe diameter versus initial pressure model B.
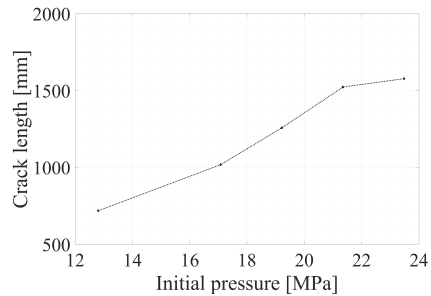

Figure 5.20: Crack length versus initial pressure model B.

For model B, where the cohesive zone was defined using partitioning, the results were quite different from model A. Both the diameter expansion and the crack length were larger for this model.

The diameter expansion, defined as the difference in measured diameter divided by original diameter, is seen in Figure 5.17. The biggest diameter expansion is observed for element size 10 mm, while a decrease of diameter expansion is observed for increasing element sizes. Figure 5.18 shows the measured crack length for the different element sizes, and how the crack propagation increases with increasing element size.

The resulting diameter expansion for varied initial pressure can be seen in Figure 5.19. The diameter expansion is quite high for all pressures run, but especially when the pressure is increased. The highest initial pressure run was 1.1 times the original as this lead to a diameter expansion of almost 30 %. The crack length for the different initial pressures is seen in Figure 5.20. Like for model A, the crack length seems to increase almost constantly for increasing pressures. The crack length is longer for this model.

Comparisons of model A and model B

As the results prove, the different models gave quite different results. As the models are identical apart from the modelling of the cohesive zone, there is no apparent reason found for this. To investigate this further, the Kahn CZ validation model explained in section 5.3, was changed so that the cohesive layer was defined in the same way as for pipe model A, i.e. using a tie constraints. The response was exactly the same as for the curves representing the CZ simulation in Figure 5.8, so this should be investigated further.

Common for both models is they are both able to simulate a running fracture. The difference is the length of the fracture and the diameter expansion. Based on the results from Schneider et al. (Scheider et al., 2014), the pipe should not expand much for the pressure found in section 5.4.2, and model A seems to represent the crack propagation best in that regard.

Also observed for both models is that the crack propagation measured is very dependent on the mesh size used in the model. The measured plastic dissipation is higher for the crack that propagates the shortest and lowest for the crack that propagates the longest, indicating that energy is lost to plastic dissipation that makes the crack propagate less. They varying mesh size may also contribute to a varying ability to represent bending. This limits the element size as it should not be too big, neither too small, in order to represent the right amount of bending while the plastic dissipation is correct.

A shell element model could also have been carried out. Different attempts were made to establish a shell element model, both defining a cohesive zone instead of using cohesive elements, and also connecting cohesive solid elements to shell elements using a shell-to-solid coupling. These proved difficult to make function properly in Abaqus. However, when running models with only solid elements, the computational time was actually very low. The 5 mm model using tie constraint had a CPU time of 1294 seconds, while the 30 element model only took 42 seconds. It was decided that the cohesive zone was considerably easier to define using only solid elements and that the surface connection was better represented by a solid model. Because of this and low CPU time, the solid element model was used in the previous parameter study.

Increasing the running time
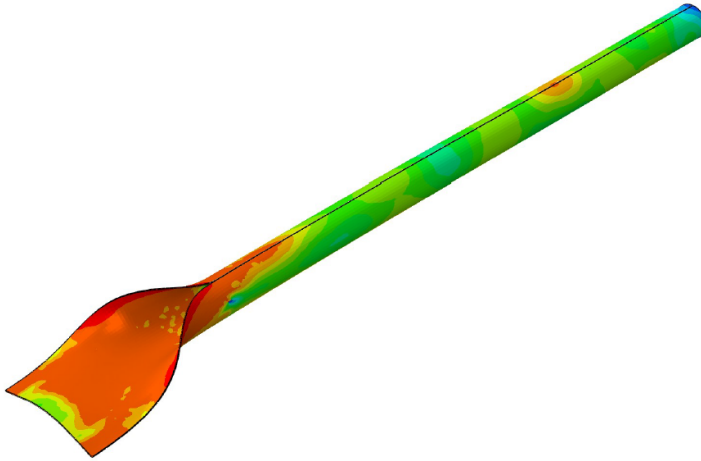
Figure 5.21: Model of pipe with element size 20 mm and initial pressure of 21.35 MPa after 2.5 millisecond.

Figure 5.21 shows model A with a mesh size of 20 mm run longer after 0.0025 seconds. The end of the pipe was locked with Z-symmetry, and the analysis was run for 0.005 seconds instead of 0.001 seconds. The result was that the part where the crack had passed deformed considerably. This is a weakness with the pressure model used in this study, as the pressure is put on the surfaces and is constant for the whole model, even after the crack has passed. Schneider et al. used a pressure decay dependent of the crack tip to describe the pressure, and for this case that would be a better model of the load case than the simplification used in this study (Scheider et al., 2014). In the studies done by Nordhagen et al. (Nordhagen et al., 2012), the crack propagated to a distance of around 1 meter after 0.005 seconds. In this model with mesh size 20 mm, Figure 5.21, the crack has propagated double that distance. However, when running the model with smaller elements of size 15 mm, the crack propagated close to 1 meter after 0.005 seconds.

5.6 Model of pipe using GTN

A section of the pipe was also modelled using only the GTN material model, using the material properties of the steel and GTN parameters found in chapter 3. The dimensions were the same as the dimensions of the CZ model of the pipe presented in Section 5.4.2, but only 2 meters was modelled. To be able to run the model with GTN without the CPU time becoming too high, only a small section around the crack path was modelled with small elements. Still, the mesh size that GTN was calibrated against would lead to a tremendous amount of elements, and an element size of 0.5 mm was chosen instead of 0.05 mm. This was considered to be all right in this case, as the simulation was done more to study the response using GTN rather than getting exact results. The elements in the rest of the model

were larger as the failure would not occur here but had three elements over the thickness to represent bending. The method used to get the different mesh sizes was to model two different parts and tie them together using tie constraint. One end of the Pipe can be seen in Figure 5.22a, and a close up of the mesh in the crack path is seen in Figure 5.22b. At the end of the pipe, a crack of length one diameter was modelled to initiate crack growth. The applied pressure and step time were the same as for the numerical model using cohesive elements.

(a)   (b)
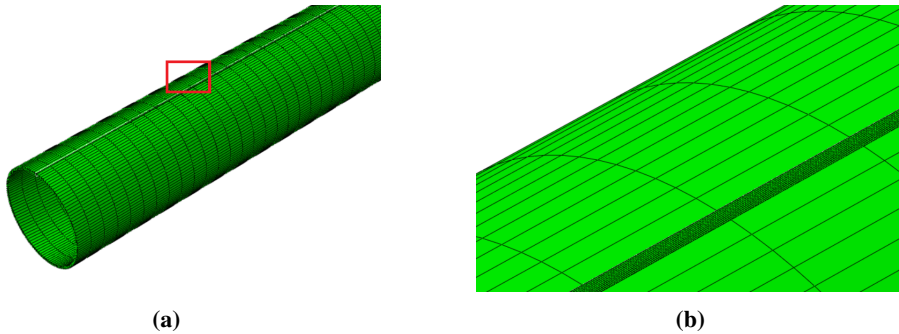
Figure 5.22: a) End of the modelled pipe using GTN **b)** Close up of the mesh used in the crack path of the GTN model, represented by the red frame in **a)**.

Figure 5.23 shows the deformed pipe at the end of the analysis. The model shows that the crack has started to develop into the pipe and the stress distribution in the model.
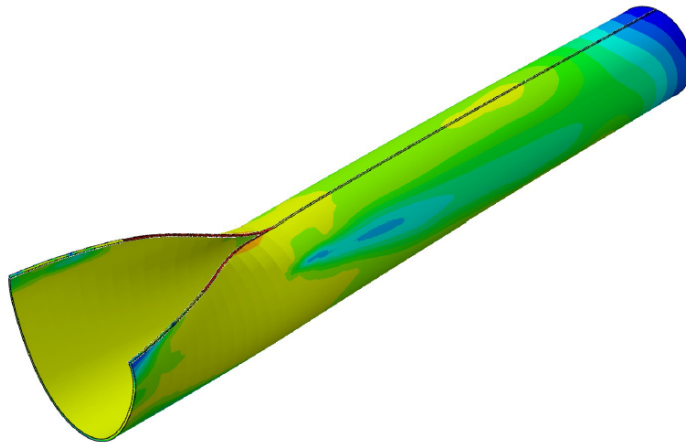
Figure 5.23: Deformation of numerical model of pipe using Gurson.

As the chosen mesh size in the crack path is too big compared to the calibrated mesh size, the results from the analysis cannot be used for exact results from the analysis. The GTN model is very mesh-sensitive, and using elements too large will often lead to non-

conservative results, and different void nucleation. Still, it gives an idea of how the crack develops in the pipe.

An interesting phenomenon that is observed in the model is the occurrence of tunnelling. As described in 4.1.2, cracks will often occur by tunnelling, and some discoveries about tunnelling are discussed in chapter 4. Figure 5.24 shows close-ups of the crack, cut in the XY-plane of different stages of the analysis. As the figures demonstrate, tunnelling does occur all the way through the analysis. The deformation in the rest of the model is small, and for this load case, a diameter expansion of 0.54% is observed.

| (a) | (b) | (c) |
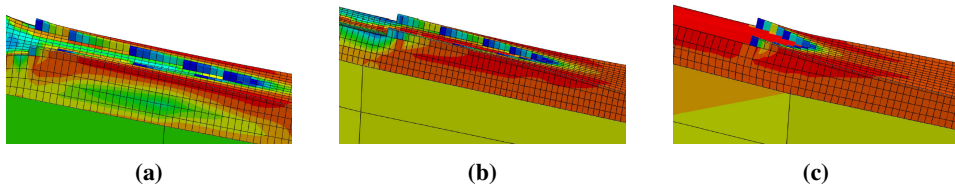
Figure 5.24: Close ups of tunneling in the numerical GNT model of the pipe for **a)** early in the analysis, **b)** middle og the analysis and **c)** end of analysis.
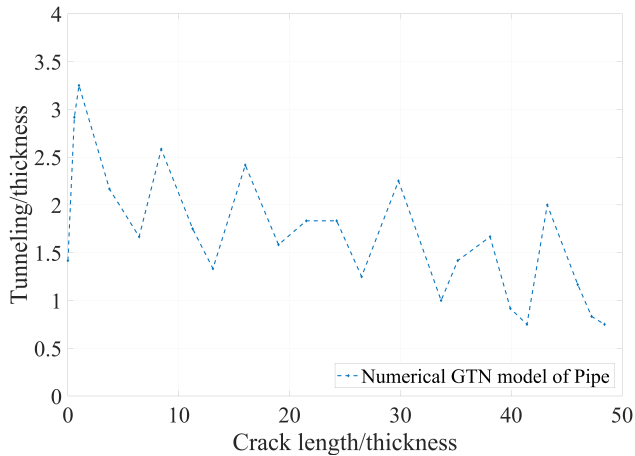
Figure 5.25: Plot illustrating the relation between the length of the tunneling vs the crack length, divided by the thickness 6 mm.

Figure 5.25 shows a plot illustrating the measured tunnelling length versus the crack length of different stages of the analysis. As is seen, the length of the tunnelling varies a great deal through the analysis, showing less consistent results than the similar plot for the Kahn tests found in section 4.2.4. Reasons for this could be because of the larger mesh-size chosen in the analysis, as the GTN model is highly mesh sensitive. The load is also applied as a pressure on the inside surface here, while for the Kahn test the load is applied

as a vertical force. Still, the plot in Figure 5.25 does show that the average tunnelling length is slightly increasing at first and then decreasing. Also for this case, a correlation between crack tunnelling and the velocity is seen, indicating that tunnelling affects the propagation of the crack.

Comparing the CZ and the GTN model will be difficult, as the results from the analysis with the CZ model have proven to be dependent on the global mesh size, and further studies should be focused on finding the optimal mesh size for the CZ model. The measured crack length of the GTN model was 288.67 mm, meaning that compared to the crack length of model A, Figure 5.16, this would correspond to a mesh size of somewhere between 10 and 15 mm.

Scheider et al. (Scheider et al., 2014) also compared CZ to GTN, but the GTN model was modelled using only one thin layer of GTN, similar to the CZ model with only one element over the thickness. They found that both were able to represent fracture well, but some weaknesses for both models were found. Also, modelling GTN with only one layer of elements would not lead to tunnelling which it was desired to observe in this study.

5.6.1 Evaluation of results

- The fracture energy for the CZ model was first calibrated and validated against the Kahn-test, and the force-elongation curve was found to represent the experiments well, even though the force was conservative.

- As no known sources have investigated the use of Kahn tearing tests for validation of the GTN model and the CZ model in X65 steel structures, no comparison to other results was done. However, when calibrating the GTN parameters using a dynamic tearing DWT test, Nonn & Kalwa were successful in describing the load-displacement curve for both a CZ model and a GTN model when comparing the results to experimental data (Nonn and Kalwa, 2013). In Figure 5.8 it can be seen that both the CZ model and the GTN model were able to match the experimental data of the Kahn tearing test quite well. This may indicate that the use of a Kahn tearing test may be a good substitute, if further investigated, to the widely used drop-weight tearing test when investigating the behaviour of X65 steel.

- The CZ model seems to be able to represent a running fracture quite well, the crack developing along the crack path as desired. The parameters calibrated based on the GTN model seem like a good starting point for further calibrations of CZ model parameters, but some refinement could be done in regards to calibration against the Kahn test. The calibration for the parameters is done based on an article by (Hutchinson and Nielsen, 2012), and they have done more studies to find the fracture energy. Further studies could be done on the calibration of the fracture and nominal stress criterion for the CZ model.

- The two different ways to model the cohesive zone also proved to give very different results. Common for both models was that the results seemed to be very dependent on the mesh size. This should be studied further, and the best relation between the mesh size and plastic deformation should be found. The size of the cohesive elements alone was proven to have little effect on the final results.

- For model A, an initial pressure of up to 1.5 times the pressure found from the studies by Schneider et al. (Scheider et al., 2014) were shown not to affect the diameter expansion too much. Meaning the pipe could handle cases of higher pressure due to imperfections in the fluid that would create higher stresses. However, the crack propagation also increased with increasing pressure.

- For model B, the diameter expansion was larger for all cases of applied pressure, and the crack-length was higher as well. Further studies should be done on the effect of using tie constraints versus partition to define the cohesive properties. Model A seems to correspond well with numerical models made in other studies, and the same method was used to model the GTN model.

- When comparing model A to the GTN model, model A seems to represent the crack in a similar way as the GTN model, but further comparisons are difficult because of the mesh dependency of the CZ model, and the too large elements used in the GTN model for simplification. The crack length found for the GTN model would correspond to a mesh size between 10-15 mm for model A.

- The CPU time for the CZ models is very short, meaning there is much potential using the CZ model if the ultimate mesh-size and loading conditions can be found. Studies using shell elements could also be carried out.

Chapter 6

Conluding remarks

The objective of this paper was to present a methodology that can be used for the assessment of pipeline fracture resistance against long-running ductile fracture. This methodology consisted of several steps required for the calculation of fracture resistance curves which represented the relation between the crack velocity and the pressure level.

The GTN model parameters for the X65 steel were calibrated against the experimental results found by Hellum. It was found that the test specimen geometry was an essential factor to consider when calibrating the material model. Kahn tearing-tests were then carried out, and the GTN model parameters found were then used in a numerical model of the Kahn-tearing test. This was compared to the experimental results for validation. The GTN model parameters were then used to calibrate the fracture parameters for a CZ model, which was first validated back to the Kahn test. The CZ model parameters were then used to model a section of a pipe where the crack path was known, and a parameter study on mesh size and pressure was performed on different CZ models of the pipe. A GTN model of the pipe was also established and compared to the CZ models.

The following conclusions can be drawn:

Specimen geometry

The GTN parameters found in chapter 3 were well able to capture the behaviour of the tensile test, being able to capture the void growth. However, with the specimens used, the results were found to be extremely sensitive to the geometry of the specimens. When using python to edge-trace the geometry of the specimens, the results were improved a great deal from the original geometry given. Establishing the correct geometry for small tensile tests is therefore important.

Validation by Kahn tearing test

Using the calibrated GTN parameters, a numerical model was able to represent a Kahn tearing-test, with a little overestimation of the forces. The deviation could be due to plas-

tification other places in the specimens during the experiments, such as around the bolt holes. As no known sources have investigated the use of Kahn tearing tests for validation of the GTN model and the CZ model in X65 steel structures, the results were an interesting part of this thesis.

Tunneling

The phenomenon of tunneling was observed in both the experimental results and the numerical model of the Kahn-test. The tunneling was found to influence the crack propagation, where more tunneling seemed to make the crack propagate slower. An increase of the tunneling was observed for the specimens in the beginning, followed by a decrease and stabilization as the crack velocity increased. The numerical model, however, seemed to overestimate the tunneling, making the crack propagate slower than the numerical model.

Numerical pipe models

For the CZ models, two parameters were calibrated based on the GTN model, the cohesive strength and the cohesive energy. Through the Kahn test validation, the CZ models were concluded to be able to represent a running fracture in a pipeline. The GTN pipe model was also successful in representing a running ductile fracture. It was found that the numerical pipe model was independent of the CZ mesh size. However, the model was very sensitive to the size of the elements outside the CZ. The measured plastic dissipation was higher for the small elements and lower for the large elements, indicating that energy is lost to plastic dissipation when the element size decreases. This may be the reason for the varying results due to element size, and finding an optimal element size that contribute to the right amount of plastic dissipation, while at the same time being able to represent bending is therefore required.

6.0.1 Further work

Based on the results found in this thesis, the following work is suggested:

- Create a numerical model of a pipe where the pressure is applied as a function of the position of the crack tip, where the method used by Schneider et al. may be a good option (Scheider et al., 2014).

- Validating a numerical pipe model by comparing the results to a fluid-structure model, as such models seem to describe the crack propagation well, to find whether the FE model can predict the running ductile fracture behaviour correctly.

- Developing a non-local GTN model to avoid mesh sensitivity.

- Further studies could be done on the calibration of the fracture and nominal stress criterion for the CZ model.

Bibliography

A. McClintock, F., 1968. A criterion for ductile fracture by the growth of holes. Journal of Applied Mechanics.

Abaqus, 2016. Abaqus Analysis User's Guide. `http://130.149.89.49:2080/v2016/books/usb/default.htm`, [Online: 10.06.2018].

Anderson, T., 2005. Fracture Mechanics: Fundamentals and Applications, Third Edition. Taylor & Francis.

Aursand, E., Dumoulin, S., Hammer, M., Lange, H., Morin, A., Munkejord, S., Nordhagen, H., 2016. Fracture propagation control in co2 pipelines: Validation of a coupled fluid–structure model. Engineering Structures.

Belostosky, A. M., Akimov, P. A., Kaytukov, T. B., Afanasyeva, I. N., Usmanov, A. R., Scherbina, S. V., Vershinin, V. V., 2014. About finite element analysis of fluid – structure interaction problems. Procedia Engineering.

Chegg, 2018. Longitudinal Stress In Thin-walled Cylinders. `https://www.chegg.com/homework-help/definitions/longitudinal-stress-in-thin-walled-cylinders-5`, [Online: 11.06.2018].

Cleaver, R., Cumber, P., 2000. Modelling pipeline decompression during the propagation of a ductile fracture. Institute of Chemical Engineers.

Dawicke, D., Newman, J., Bigelow, C., 1995. Three-dimensional ctoa and constraint effects during stable tearing in a thin-sheet material. Fracture mechanics.

Dr Alexander Völling, Dr Marion Erdelen-Peppler, D. C. K. H. B. B. O. H. M., 2013. Numerical approach for crack-arrest prediction by fem. 6th International Pipeline Technology Conference.

eCorr, 2018. eCorr documentation. `http://folk.ntnu.no/egilf/ecorr/doc/definitions/strain/logstrains.html`, [Online: 09.04.18].

Gullerud, A., Dodds, R., Hampton, R., Dawicke, D., 1999. Three-dimensional modeling of ductile crack growth in thin sheet metals: computational aspects and validation. Engineering Fracture Mechanics.

Gurson, A. L., 1977. Continuum theory of ductile rupture by void nucleation and growth: Part i—yield criteria and flow rules for porous ductile media. Journal of Engineering Materials and Technology.

Hellum, G. M., 2017. Ductile-brittle transition in offshore steel, *PhD thesis, Norwegian University of Science and Technology*.

Holmen, J. K., Frodal, B. H., Hopperstad, O. S., Børvik, T., 2017. Strength differential effect in age hardened aluminum alloys. International Journal of Plasticity.

Hopperstad, O., Børvik, T., 2017a. Impact mechanics – part 1.

Hopperstad, O., Børvik, T., 2017b. Impact mechanics – part 2.

Hutchinson, J. W., Nielsen, K. L., 2012. Cohesive traction-separation laws for tearing of ductile metal plates.

Irgens, F., 1996. Fasthetslære:. Tapir forlag.

James, M., Newman, J., 2003. The effect of crack tunneling on crack growth: experiments and ctoa analyses. Engineering Fracture Mechanics.

Lan, W., Deng, X., Sutton, M. A., 2010. Investigation of crack tunneling in ductile materials. Engineering Fracture Mechanics.

Mahgerefteh, H., Brown, S., Denton, G., 2012. Modelling the impact of stream impurities on ductile fractures in co2 pipelines. Chemical Engineering Science.

Mathur, K., Needleman, A., Tvergaard, V., 1996. Three dimensional analysis of dynamic ductile crack growth in a thin plate. Journal of the Mechanics and Physics of Solids.

Nonn, A., Kalwa, C., 2013. Analysis of dynamic ductile fracture propagation in pipeline steels: A damage-mechanic's approach. 6th International Pipeline Technology Conference6th International Pipeline Technology Conference.

Nordhagen, H., Dumoulin, S., Gruben, G., 2014. Main properties governing the ductile fracture velocity in pipelines: A numerical study using an (artificial fluid)-structure interaction model. Procedia Materials Science.

Nordhagen, H., Kragset, S., Berstad, T., Morin, A., Dørum, C., Munkejord, S., 2012. A new coupled fluid–structure modeling methodology for running ductile fracture. Computers Structures.

Nordhagen, H., Munkejord, S., Hammer, M., Gruben, G., Fourmeau, M., Dumoulin, S., 2017. A fracture-propagation-control model for pipelines transporting co2-rich mixtures including a new method for material-model calibration. Engineering Structures.

Oh, C.-K., Kim, Y.-J., Baek, J.-H., Kim, W.-S., January 2007. Development of stress-modified fracture strain for ductile failure of api x65 steel. International Journal of Fracture.

Pauwels, J., Lamberty, A., Schimmel, H., 1998. Homogeneity testing of reference materials. Accreditation and Quality Assurance.

PMinternational, S., 2018. API 5L X Grades. `http://www.api5lx.com/api5lx-grades/`, [Online: 09.04.18].

Rice, J., Tracey, D., 1969. On the ductile enlargement of voids in triaxial stress fields. Journal of the Mechanics and Physics of Solids.

Salve, A., Jalwadi, S., 05 2015. Implementation of cohesive zone in abaqus to investigate fracture problems.

Scheider, I., 05 2018. Cohesive model for crack propagation analyses of structures with elastic–plastic material behavior foundations and implementation.

Scheider, I., Nonn, A., Völling, A., Mondry, A., Kalwa, C., 2014. A damage mechanics based evaluation of dynamic fracture resistance in gas pipelines. Procedia Materials Science20th European Conference on Fracture.

Schwalbe, K.-H., Scheider, I., Cornec, A., 2013. Guidelines for Applying Cohesive Models to the Damage Behaviour of Engineering Materials and Structures. Springer-Verlag Berlin Heidelberg.

Spitzig, W., Richmond, O., 1984. The effect of pressure on the flow stress of metals. Acta Metallurgica.

Sævareid, S., 2017. Influence of precipitate-free zones on tensile ductility and tear resistance of 6000 aluminium alloys, *PhD thesis, Norwegian University of Science and Technology*.

Tvergaard, V., 1981. Influence of voids on shear band instabilities under plane strain conditions. International Journal of Fracture.

Tvergaard, V., 1982. On localization in ductile materials containing spherical voids. International Journal of Fracture.

Tvergaard, V., Needleman, A., 1984. Analysis of the cup-cone fracture in a round tensile bar.

Zuo, J., Deng, X., Sutton, M., Cheng, C.-S., 2004. Crack tunneling: Effect of stress constraint 255.

Appendix

Appendix 1: Edge Tracing - Python Code

```python
import numpy as np
import matplotlib.pyplot as plt
from scipy import ndimage as ndi
from skimage import feature
import cv2
import os


work_dir = os.getcwd()
# The specimen image must be provided:
specimen_img = "R2_specimen.PNG"
#specimen_img = "R08_specimen.PNG"
#specimen_img = "Vnotch_specimen.PNG"
# ... other images if so desired...

img_path = work_dir + "\\" + specimen_img



#-----------------------------------------------------------------
# User must define the size of the specimen (in e.g. [mm]):
#-----------------------------------------------------------------
DIAMETER_R2     = 0.003
#DIAMETER_R08   = 0.003
#DIAMETER_V     = 0.003
# ... additional specimens if so desired..
# Choose the current specimen:
DIAMETER = DIAMETER_R2

OUTER_DIAMETER_R2   = 0.005
#OUTER_DIAMETER_R08 = 0.005
#OUTER_DIAMETER_V   = 0.005
# ... additional specimens if so desired..
# Choose the current specimen:
```

```
OUTER_DIAMETER = OUTER_DIAMETER_R2

SPECIMEN_LENGHT = 50.


#-----------------------------------------------------------------
# Import the image:
#-----------------------------------------------------------------
img = cv2.imread(img_path,0)
#plt.figure()
#plt.imshow(img, 'gray')

#-----------------------------------------------------------------
# Zoom in on the desired part of the image to edge-trace:
#-----------------------------------------------------------------
rows,cols = np.shape(img)
image = img[int(rows//2):int(rows), \
       + int(cols//1.71):int(cols//1.32)]

#-----------------------------------------------------------------
# Edge trace the specimen on the image:
#-----------------------------------------------------------------
# Tweak these limits for even better results. Depends on the image..
upper_lim_gradient = 100
Lower_lim_gradient = 200

edges = cv2.Canny(img, upper_lim_gradient, upper_lim_gradient)
x_points = []
y_points = []
for x,row in enumerate(edges):
    for y,col in enumerate(row):
        if col != 0:
            x_points.append(x)
            y_points.append(y)
# The edge-coordinates are now stored as x- and y-values.

# Plot the points in order to validate:
#plt.figure()
#plt.plot(x_points,y_points)
```

```python
#----------------------------------------------------------------
# Split the edge-traced image into an upper and lower part:
#----------------------------------------------------------------
mid_val = np.mean(y_points)
lower = []
upper = []
for x_val, y_val in zip(x_points, y_points):
    if y_val > mid_val:
        upper.append((x_val, y_val))
    else:
        lower.append((x_val, y_val))
x = [x for x,_ in lower]
y = [y for _,y in lower]
#plt.plot(x, y, 'r')
x = [x for x,_ in upper]
y = [y for _,y in upper]
#plt.plot(x, y, 'r')


#----------------------------------------------------------------
# Find the diameter, in order to scale the edges:
#----------------------------------------------------------------
y_low_point = min([y for _,y in upper])
low_index = np.argmin([y for _,y in upper])
x_low_point = upper[low_index][0]
y_high_point = max([y for _,y in lower])
high_index = np.argmax([y for _,y in lower])
x_high_point = lower[high_index][0]


#----------------------------------------------------------------
# Scale the specimen:
#----------------------------------------------------------------
scaling = abs(y_high_point - y_low_point) / DIAMETER
# Upper redge:
x = np.array([x for x,_ in lower])
y = np.array([y for _,y in lower])
x_low = x/scaling
y_low = y/scaling
# Lower edge:
x = np.array([x for x,_ in upper])
y = np.array([y for _,y in upper])
x_upper = x/scaling
y_upper = y/scaling
#plt.figure()
#plt.plot(x_low, y_low, x_upper, y_upper)
```

```python
#------------------------------------------------------------
# The specimen are now scaled, but the edges are not smooth.
# In order to obtain a smooth edge, a n'th order polynomial
# is fitted to the specimen edge:
# Here, the upper edge is chosen:
#------------------------------------------------------------
# Choose the order of the polynomial here:
n_order = 12

edge_val = np.mean(y_upper)
x_new = []
y_new = []
for x_val, y_val in zip(x_upper,y_upper):
    if y_val < edge_val:
        x_new.append(x_val)
        y_new.append(y_val)

# Manual tweaking to ensure that only the desired part of the
# specimen is fitted (the notch):
x_new = x_new[110:-3]
y_new = y_new[110:-3]
x_new = [x_new[0]] + x_new + [x_new[-1]]
y_new = [edge_val] + y_new + [edge_val]
#plt.figure()
#plt.plot(x_new, y_new)

solution_x = list(np.linspace(x_new[0], x_new[-1], 200))
z = np.polyfit(x_new, y_new, n_order)
p = np.poly1d(z)

# CALIBRATED EDGE:
x_high_solution = solution_x
y_high_solution = p(solution_x)
#plt.plot(x_high_solution, y_high_solution)




#------------------------------------------------------------
# The notched edge has been traced, but the edges of the entire
# specimen is yet to be determined:
#------------------------------------------------------------
min_val = min(y_high_solution)
y_high_solution = y_high_solution - min_val + DIAMETER/2.
y_high_solution = list(y_high_solution)
```

```python
x_high_solution = list(x_high_solution)
max_val_r = y_high_solution[-1]
max_val_l = y_high_solution[0]

# Find the necessary extension of the notch:
diff_right = OUTER_DIAMETER/2. - max_val_r
diff_left = OUTER_DIAMETER/2. - max_val_l

# Center of specimen:
x_ind = np.argmin(y_high_solution)
x_val = x_high_solution[x_ind]

# Create sharp right edge:
slope_right = (y_high_solution[-1] - y_high_solution[-2]) \
        +  / (x_high_solution[-1] - x_high_solution[-2])
delta_x = diff_right / slope_right
y_high_solution.append(OUTER_DIAMETER/2.)
x_high_solution.append(x_high_solution[-1] + delta_x)

# Create sharp left edge:
slope_left = (y_high_solution[0] - y_high_solution[1]) \
        +  / (x_high_solution[0] - x_high_solution[1])
delta_x = diff_left / slope_left
y_high_solution = [OUTER_DIAMETER/2.] + y_high_solution
x_high_solution = [x_high_solution[0] + delta_x] + x_high_solution




# Create the rest of the specimen:
abaqus_lines = ((x_high_solution[0], y_high_solution[0]), \
    +  (x_val - SPECIMEN_LENGHT/2., OUTER_DIAMETER/2.), \
    +  (x_val - SPECIMEN_LENGHT/2., 0), \
    +  (x_val + SPECIMEN_LENGHT/2., 0), \
    +  (x_val + SPECIMEN_LENGHT/2., OUTER_DIAMETER/2.), \
    +  (x_high_solution[-1], y_high_solution[-1]))
temp = [(pair[1], pair[0]) for pair in abaqus_lines]
abaqus_lines = tuple(temp)
```

```python
#-----------------------------------------------------------------
# Write it to a python script ready to run from Abaqus:
#-----------------------------------------------------------------
filepath = work_dir + "\\" + "Input_to_Abaqus.py"
with open(filepath,'w') as file:
    file.write("from abaqus import *\n")
    file.write("from abaqusConstants import *\n")
    file.write("from caeModules import *\n")
    file.write("from driverUtils import executeOnCaeStartup\n")
    file.write("s = "\
        + "mdb.models['Model-1'].ConstrainedSketch(name="\
        + "'__profile__', sheetSize=0.01)\n")
    file.write("g, v, d, c = s.geometry, s.vertices, "\
        + "s.dimensions, s.constraints\n")
    file.write("s.setPrimaryObject(option=STANDALONE)\n")

    # CREATE THE SPLINE POINTS:
    points = []
    for x,y in zip(x_high_solution, y_high_solution):
        points.append((y,x))
    points = tuple(points)
    file.write("s.Spline(points={0})\n".format(points))
    for point1, point2 in zip(abaqus_lines[:-1],\
    +  abaqus_lines[1:]):
        file.write("s.Line(point1={0},"\
        +  "point2={1})\n".format(point1, point2))
    file.write("s.ConstructionLine(point1=(0.0, -100.0),"\
        +  "point2=(0.0, 100.0))\n")
    file.write("p = mdb.models['Model-1'].Part(name="\
        +  "'Edge_Traced', dimensionality=AXISYMMETRIC,"\
        +  "type=DEFORMABLE_BODY)\n")
    file.write("p.BaseShell(sketch=s)\n")
    file.write("s.unsetPrimaryObject()\n")
    file.write("session.viewports['Viewport: 1'"\
        +  "].setValues(displayedObject=p)\n")
    file.write("del "\
        +  "mdb.models['Model-1'].sketches['__profile__']\n")
    file.write("\n"*2)
```